ARCTIC
VOL. 78, NO. 1 (MARCH 2025) P. 56–76
https://doi.org/10.14430/arctic82154

Assessing Coastal Wetland Carbon and Mineral Accumulation Response to Changing Climate, Cape Espenberg, Alaska

Lindsey Smith,[1, 2] Chris Maio,[1] Nancy Bigelow[3] and Meagan Eagle[4]

(*Received 20 April 2024; accepted in revised form 4 December 2024*)

ABSTRACT. The Arctic is experiencing warming and ecological shifts due to climate change and the compounding effects of polar amplification. Arctic Alaskan coastal marsh environments, such as the Cape Espenberg barrier beach system, offer an opportunity to determine the carbon cycle response to changing climate by examining sediment records that have been preserved through time as shoreline-parallel, linear geometry prograding geomorphic features. This study determines the carbon and mineral accumulation trends in marsh environments at Cape Espenberg for both paleo (~776 CE to 1850 CE) and modern (post-1850 CE) time frames. A comprehensive physical and chemical dataset, including radioisotope (^{137}Cs, ^{210}Pb, ^{14}C), stable isotope (δ^{13}C), element concentration (%C, %N, C:N), and dry bulk density, has been built for several sediment cores. Results indicate that carbon and mineral accumulation rates have increased from paleo to modern times, potentially because of better growing and preservation conditions for organic matter in a modern climate. Paleoclimate trends in the Medieval Climate Anomaly (MCA) and warm periods interspersed within the Little Ice Age (LIA) also correlate with greater contributions of wetland organic matter, as evidenced by lighter δ^{13}C values. Cold climate periods within the LIA correlate with increased aquatic organic matter sourcing and heavier δ^{13}C values, with some spikes of wetland sources interspersed throughout the LIA. Future temperatures are predicted to rise with global climate change, which may continue to expand carbon stores in Arctic coastal wetland sediments. This has been observed in the swale environments at Cape Espenberg, where increasingly favourable growing and soil-preservation conditions (i.e. wet/anoxic soils and lower salinity to limit organic material decay, higher temperatures to promote growth) are increasing the carbon storage within Arctic coastal carbon reservoirs.

Keywords: paleoclimate; wetland; radioisotope; stratigraphy; radiocarbon

RÉSUMÉ. L'Arctique connaît un réchauffement et des glissements écologiques en raison du changement climatique et des effets conjugués de l'amplification polaire. Grâce aux dépôts sédimentaires préservés au fil du temps sous la forme de caractéristiques géomorphologiques progradées à géométrie linéaire parallèles à la côte, les milieux marécageux de la côte alaskienne de l'Arctique, comme celui du système de cordon littoral du cap Espenberg, offrent un aperçu de la manière dont le cycle de carbone évolue face au changement climatique. Cette étude détermine les tendances d'accumulation de carbone et de minéraux dans les milieux marécageux de cap Espenberg pour la période paléoclimatique (~776 EC à 1850 EC) et la période moderne (après 1850 EC). Un ensemble de données physiques et chimiques exhaustif, comprenant notamment des radio-isotopes (^{137}Cs, ^{210}Pb, ^{14}C), des isotopes stables (δ^{13}C), des concentrations d'éléments (%C, %N, C:N) et des masses volumiques en vrac solide a été préparé pour plusieurs carottes de sédiments. Selon les résultats, les taux d'accumulation de carbone et de minéraux ont augmenté entre la période paléoclimatique et la période moderne, peut-être en raison des meilleures conditions de croissance et de préservation de la matière organique dans un climat moderne. Les tendances paléoclimatiques de l'optimum climatique médiéval (OCM) et les périodes de réchauffement entrecoupées du petit âge glaciaire (PAG) correspondent également à de plus grands apports en matières organiques de terres humides, comme en attestent les valeurs moins élevées de δ^{13}C. Les périodes de climat froid du PAG sont liées à un apport accru de sources de matières organiques aquatiques et à de plus grandes valeurs de δ^{13}C, avec certaines pointes de sources en milieu humide intercalées tout au long du PAG. En raison du changement climatique mondial, les températures devraient monter à l'avenir, ce qui pourrait continuer d'intensifier les réserves de carbone des sédiments côtiers en milieu humide de l'Arctique. Cela a été observé dans les baissières du cap Espenberg, où les conditions de croissance et de préservation du sol de plus en plus favorables (c'est-à-dire les sols humides et anoxiques et une moins grande salinité ayant pour effet de restreindre la dégradation des matières organiques, assortis de températures plus élevées favorisant la croissance) intensifient le stockage de carbone dans les réservoirs de carbone côtiers de l'Arctique.

Mots-clés : paléoclimat; terres humides; radio-isotope; stratigraphie; radiocarbone

Traduit pour la revue *Arctic* par Nicole Giguère.

[1] Arctic Coastal Geoscience Laboratory, 900 Yukon Drive, Reichardt Building, University of Alaska Fairbanks, Fairbanks, Alaska 99775, USA
[2] Corresponding author: lsmith131@alaska.edu
[3] Arctic Quaternary Center, 900 Yukon Drive, Reichardt Building, University of Alaska Fairbanks, Fairbanks, Alaska 99775, USA
[4] U.S. Geological Survey, Woods Hole Coastal and Marine Science Center, 384 Woods Hole Road, Woods Hole, Massachusetts 02543, USA

INTRODUCTION

Mean annual Arctic warming is approximately 1.9 times that of the global mean (Serreze and Barry, 2011). Observed changes in the Arctic include widespread cryosphere degradation with mass loss from glaciers and ice sheets (IPCC, 2019, 2023); decreased sea ice duration, extent, and thickness (Chapin et al., 2005; Mahoney et al., 2014; Farquharson et al., 2018; IPCC, 2019; IPCC, 2023); record-high global average permafrost temperatures across polar and high mountain regions (IPCC, 2019); and tundra vegetation conversion to shrubs and trees (Tape et al., 2006; Myers-Smith et al., 2015).

There is a paucity of information regarding the geomorphic and ecological responses of Arctic coastal marsh environments to a warming climate (Ford and Pearce, 2009; Wassmann et al., 2010; Seifollahi-Aghmiuni et al., 2019). Vegetated coastal environments (seagrasses, mangroves, and salt marshes) hold large stores of pedologic and biotic carbon by removing CO_2 from the atmosphere during photosynthesis and storing carbon as sedimentary organic matter for extended time scales within anoxic environments (Chmura et al., 2003; Ward, 2020). The high rates of carbon storage in coastal wetland systems have led to their inclusion in national assessments of nature-based climate solutions (Fargione et al., 2018). However, future persistence is uncertain because of large areal losses of these systems from erosion and submergence, uncertain ecosystem response to sea-level rise, and human modifications (Holmquist et al., 2018; Murray et al., 2022; Osland et al., 2022). The majority of research to date has focused on coastal wetlands outside of the Arctic, despite 12% (or 3.5 million km^2) of global coastal wetlands occurring in this region (Flagstad et al., 2018; Tootchi et al., 2019; Kåresdotter et al., 2021). Knowledge of carbon storage rates within Alaskan Arctic coastal wetlands is needed to assess the potential carbon stock and rate of atmospheric CO_2 removal characteristic of these environments.

This study determines soil organic carbon storage rates and carbon sources across a prograding barrier ridge and swale system at Cape Espenberg, Alaska, at the northernmost tip of the Seward Peninsula over the past ~1500 years (Fig. 1). Sediment cores were collected at four locations across Cape Espenberg to assess environmental changes in the prograding barrier from late Holocene (~2200 BCE) to modern times (post-1850 CE). We refer to modern periods as those after 1850, when atmospheric CO_2 levels began to rise, and the period prior to 1850 as paleo, in an effort to capture the biogeochemical changes across the shift in climate. Age models for the cores were developed using ^{210}Pb and ^{14}C dates; soil carbon sources and carbon burial rates were derived from $d^{13}C$ and bulk C measurements. Wetland responses to changing climate, sea level, and hydrologic regimes typically involve complex feedbacks including changes in plant productivity and soil organic matter preservation in response to storm flooding and salinization, mineral deposition, and erosion (Jordan and Mason, 1999; O'Donnell et al., 2012; McLaughlin and Webster, 2014; Swindles et al., 2016). Therefore, sediment records were assessed within the context of pre-existing Arctic climate and storm proxy data to decipher how rates have changed during past climate events associated with both abnormally warmer and colder conditions, such as the Medieval Climate Anomaly (MCA) and Little Ice Age (LIA). We also assessed the impact of recent warming and storm events to inform our understanding of how changing conditions influenced carbon and mineral accumulation in Arctic coastal wetlands and of potential future changes as the climate evolves.

STUDY AREA

Late Holocene and Physiographic Setting

The Cape Espenberg coastal barrier ridge complex sits on the Arctic Circle and is located on the eastern coast of the Chukchi Sea within the semi-sheltered Kotzebue Sound (Fig. 1). The study site encompasses the easternmost tip (~2 km wide) of the cape's barrier beach system. Cape Espenberg is part of the Bering Land Bridge National Preserve, which encompasses 2.7 million acres (U.S. NPS, 2015) in the northwest section of the Seward Peninsula (Willingham, 2018). The cape has been inhabited by Indigenous Peoples for at least 4500 years; they are living today in regional villages including Shishmaref and Deering (Giddings, 1967; Giddings and Anderson, 1986; Schaaf, 1988; Harritt, 1994; Urban et al., 2016; Norman et al., 2017). The cape exhibits multiple permafrost features that can be seen from satellite imagery and field observations, including earth hummocks, frost boils, palsas, ice wedge polygons, and thermokarst lakes and ponds (Plug, 2003). Ground-penetrating radar data shows that the permafrost is continuous (1–2 m below surface) along the cape, but permafrost features are most prominent in low-elevation swales (Plug, 2003). The presence of permafrost creates a perched freshwater table under most of the spit (Plug, 2003; O'Donnell et al., 2012).

Previous work has documented that the barrier has continuously prograded seaward for approximately 5000 years (Mason, 1990; Mason et al., 2020), providing a system that is uniquely situated to preserve a sedimentary record of past environmental change (Jordan and Mason, 1999). Progradation is due to both the relatively stable sea levels during the late Holocene and an abundant sediment supply (Mason et al., 1997). The Yukon River is a major source of sediment for Cape Espenberg; annual sediment flux to the Yukon River delta is 54 to 68 metric tonnes (Brabets et al., 2000; Dornblaser and Striegl, 2009). A portion of this sediment is transported northward by the Alaska Coastal Current and then along the Seward Peninsula by a longshore current (Giddings, 1952; Gärtner et al., 2013; Smith et al., 2017).

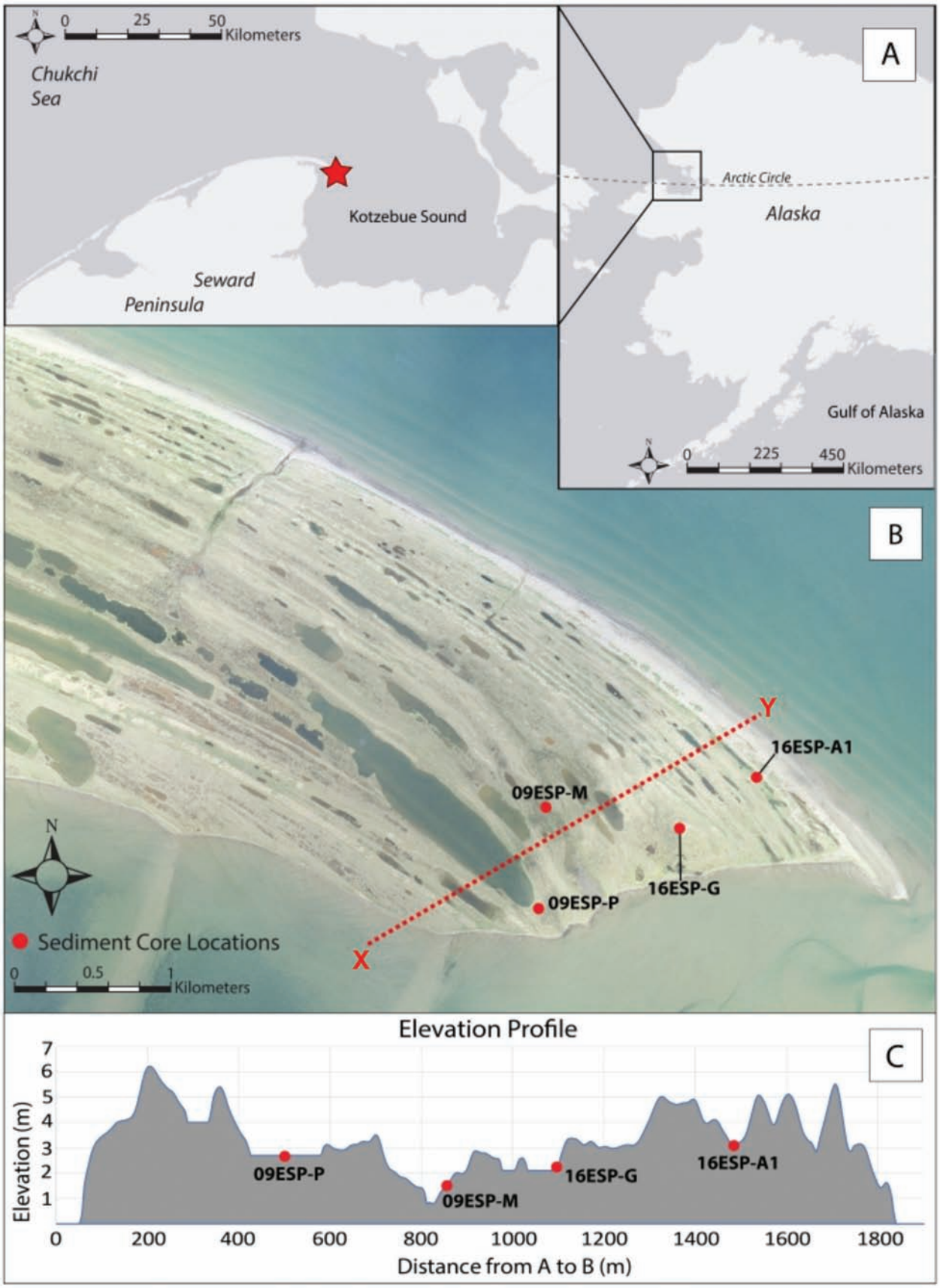

FIG. 1. A) Maps of Alaska and the northern Seward Peninsula region; B) Study site locations (red dots) and elevation transect (red dashed X–Y line); C) Elevation profile with approximate locations of the cores (red dots). Greyscale map in insert A from State of Alaska, Esri, TomTom, Garmin, FAO, NOAA, USGS, EPA, NPS, USFWS. Coloured map in insert B from 2010 TerraMetrics.

At Cape Espenberg, late Holocene sea-level rise along the Seward Peninsula was approximately 0.3 mm/yr (Jordan and Mason, 2002) compared to ~1 mm/yr global mean sea-level rise (Douglas, 1991; Pirazzoli, 1991; Gornitz, 1995). Since 1880, global mean sea level has increased 21 cm to 24 cm, with an average rate of 1.4 mm/yr during the early 20th century and then increasing to 3.6 mm/yr from 2006 to 2015 (Church and White, 2011; Lindsey, 2020). Tide gauge data at Nome, Alaska, located 243 kilometres south of the study site, documents a 3.9 mm/yr sea level rise with a 95% confidence interval of ± 2.7 mm/yr between 1992 and 2020 (NOAA, 2021). This rate is closely aligned with modern global rates, indicating an acceleration in the rate of relative sea-level rise (RSLR) in northwest Alaska compared to the stability of the late Holocene. While the Cape is geologically dynamic (i.e., growing) the coastal wetlands studied here have features persistent over thousands of years.

METHODS

This paleoclimate reconstruction is based on sediment core lithology, distribution of short-lived radionuclides, and radiocarbon dating of basal peat macrofossils (i.e., terrestrial seeds, organic fragments, and wood). Age models were built from short-lived radionuclide and ^{14}C data to reconstruct sedimentation and carbon accumulation rates through time. In addition, stable carbon (C) and nitrogen (N) isotopes of soil organic matter provided information about environmental setting and organic matter provenance. Results of this study were compared to historic climatic change events including the LIA, MCA, and warming since the 1950s. For this project, accumulation rate is defined as the total vertical accumulation in millimetres per year (mm/yr) and includes both mineral and organic materials. Carbon burial rate is defined as the total carbon accumulation in grams per square metre per year ($gC/m^2/yr$). Finally, carbon stocks are defined as the total amount of organic carbon in grams contained in the total peat strata per core (e.g., core 16ESP-A1 has 14 cm of peat, thus carbon stocks were calculated down to 14 cm depth).

Coring Methods

Four sediment cores were collected from swales in peat marshes, which are semi-connected to the ocean, during field seasons in 2009 and 2016 (Table 1). A modified snow, ice, and permafrost research establishment auger (Hughes and Terasmae, 1963) was used in areas with permafrost, and a hammer corer was used for shallower, unfrozen sediments. Sediment cores were extracted in the field and placed in plastic wrap-lined acrylonitrile butadiene styrene tubes that had been split lengthwise. The tube halves were then taped shut, forming a robust core holder prior to shipping. Surface vegetation was surveyed in a three-metre radius surrounding the core site (i.e., the core location was the central point). Core location and elevation were

TABLE 1: The four sediment cores analyzed and major descriptions. Refer to subsequent tables for data summaries of elemental and physical analysis and calculations ($\delta^{13}C$, %C, DBD, gamma spectroscopy, and carbon density). All elevations are reported relative to the NAVD88 datum. Abbreviations are cal for calibrated, F3 for facies 3, CE for Common Era, prob. for probability, and MHW for mean high water.

Core ID	Core length (cm)	Depth of F3 peat (cm)	Oldest ^{14}C Age Cal CE Median prob. (cal yr)	2σ cal CE Age range (cal yr)	Oldest ^{14}C Age depth (cm)	Latitude °N	Longitude °W	Salinity (ppt)	Elevation (m)	Height above MHW (m)	Surface vegetation (listed in order of most to least abundant)
16ESP-A1	62	~14	N/A	N/A	N/A	66.5600	–163.6162	0.21	3.34	3.08	*Carex* sp. and Moss, *Caltha* sp., *Potentilla palustris*
16ESP-G	74	~28	1185	1044–1270	37	66.5583	–163.6236	0.11	2.38	2.12	*Carex* sp. or *Eriophorum* sp., Moss, *Rumex* sp. and *Salix* sp. and *Eriophorum* sp.
09ESP-M	85	~23	1010	904–1113	31	66.5593	–163.6366	N/A	2.00	1.74	*Carex* sp. or *Eriophorum* sp., *Salix* sp. and *Asteraceae* sp. and *Elymus* sp.
09ESP-P	67	~27	1520	433–639	39	66.5553	–163.6377	N/A	3.10	2.84	*Carex* sp. or *Eriophorum* sp.

measured with a real-time kinematic global navigation satellite system (RTK-GNSS). Horizontal and vertical accuracy was 10 cm or better. Cores were transported to the University of Alaska Fairbanks Arctic Coastal Geoscience Lab (~1 week unrefrigerated in transit), refrigerated at 4.4˚C upon arrival, split lengthwise, logged, and placed in polystyrene D-shaped tubes for storage in the coolers.

We examined the peat structure of each sediment core for variations in colour, texture, and organic composition. Plant macrofossils and mineral horizons (sand or silt) within peat deposits were also noted. Within sand deposits, special features such as bedding or layering, dark organic layers, wood fragments, shells, variations in colour, sharpness of contacts, and grain size were noted. Three main facies were determined for all sediment cores based on visual appearance, organic content, the presence of macrofossils, shells, and biogeochemical data (Fig. 2). These facies are laterally continuous, though they vary in thicknesses, among all cores. For each stratigraphic unit, boundaries and changes in stratigraphy were recorded in the corresponding field book using a detailed description and sketch. Field notes were transcribed into digital core logs using universal symbology (adapted from USGS, 2006 FGDC Digital Cartographic Standard).

Analytical Techniques

Radiocarbon: Midcore and basal depth ages were determined using radiocarbon analysis of terrestrial plant macrofossils from Cape Espenberg sediment core samples. Extreme care was taken when picking radiocarbon macrofossils to avoid age contamination from shells, old wood, aquatic plants, and other unidentifiable debris that might contain older carbon. Seven radiocarbon dates were determined from three of the cores (core 16ESP-A1 consisted of post-1950 CE sedimentary deposits and was not used for radiocarbon dating). A single anomalous age (i.e., post-1950 CE) from core 09ESP-M was not used in the generation of any results; we suspect modern plant/wood fragment contamination was the source of the post-1950 CE date at the sample depth of 20.5 cm. Samples were extracted from a section of the core that was 1–2 cm thick and were sieved through a 250 micron sieve and rinsed in reverse osmosis water. The material for radiocarbon dating was targeted from mid- to basal organic-rich horizons (16ESP-A1 was not sampled because it consisted of material from post-1950 CE), then selected from plant macrofossils that did not pass through the sieve, excluding wood or aquatic organics to avoid age contamination (Table 2). Samples were dried at 50˚C–55˚C and sent to the radiocarbon lab at the National Ocean Sciences Accelerator Mass Spectrometry (AMS) facility in Woods Hole, Massachusetts (WHOI, 2015), which uses a continuous flow AMS system. All reasonable radiocarbon dates were calibrated using the IntCal20 Northern Hemisphere terrestrial calibration curve in the HTML Calib version 8.2 program (Reimer et al., 2020); calibrated radiocarbon dates were included, with other measured parameters, in a comprehensive age-depth model. The radiocarbon dates are reported, as calibrated, in BCE/CE for this study.

Gamma Spectroscopy: Soil samples were analyzed via gamma spectroscopy for ^{137}Cs (half-life 30 years), ^{210}Pb (half-life 22.3 years), and supported ^{210}Pb via ^{226}Ra (Hagedorn et al., 2008; De la Cruz et al., 2011; Voltaggio and Spadoni, 2011; Baltas et al., 2018). One-centimetre-thick sections were sampled with a volumetric syringe from archived cores, dried at 55˚C–60˚C for four to seven days, and homogenized. Weights were collected after drying to determine the sediment's dry bulk density (DBD). Samples were transferred to a jar, sealed, and let sit for a minimum of three weeks to allow ^{226}Ra (e.g., supported-^{210}Pb) to come to equilibrium prior to analysis on planar-style gamma counters; ^{137}Cs, ^{210}Pb, and ^{226}Ra were assessed at 661.6, 46.5, and 352 kiloelectron-volt (keV) energies respectively. The gamma counters were calibrated to an Environmental Protection Agency standard pitchblende ore in the same geometry as the samples, and self-absorption (suppression of low-energy peaks) was corrected for by using the Cutshall et al. (1983) method. Activities of ^{137}Cs and ^{210}Pb were decay corrected to the time of collection. The unsupported ^{210}Pb detection limit was three becquerel; $^{210}Pb_{excess}$ was calculated as ^{210}Pb minus ^{226}Ra activities.

Age Models: We used age-depth modelling to determine the mineral and carbon accumulation rates for each core. Inputs to age models included ^{137}Cs peak depth (corresponding to 1963), $^{210}Pb_{excess}$ sediment activities, and ^{14}C dates for selected cores. We used R package rplum (software R version 2.5.6, rplum version 0.2.2.9), which is a Bayesian implementation of the ^{210}Pb-based constant rate of supply model and includes the previously developed rbacon (rbacon version 2.5.6) age model (Appleby, 2001; Blaauw and Christen, 2011; Aquino-Lopez et al., 2018). All cores were run with integrated ^{14}C dates ("otherdates" code), 1 cm thickness (model slice depth and sampling interval), output in years BC/AD (BCAD = TRUE code), and an s.mean of 10 (s.mean = 10 code). The other parameters used to run each model were unique to each core (see supplementary Table S1) based on the results of each trial but were still within similar ranges (except for phi.mean, which showed wide variance between the four cores).

Stable Isotope Spectrometry: To determine the carbon (vegetative) environmental response to different periods of climate, we conducted a stable isotope analysis of δ^{13}C and δ^{15}N for each sediment core. The sections of the cores that contained peat were sampled at 2 cm intervals and analyzed to determine the total carbon and nitrogen content and stable isotope signature of bulk organic material. Prior to sampling archived cores, the soil surface was cleaned with a scraping tool to remove contamination from the core-splitting process. Approximately one cubic centimetre of sediment was extracted with a metal spatula, placed in tin boats, and dried in an oven at 50˚C for 24 to 48 hours. Samples were then homogenized into a fine powder by hand with a mortar and pestle. Samples were analyzed

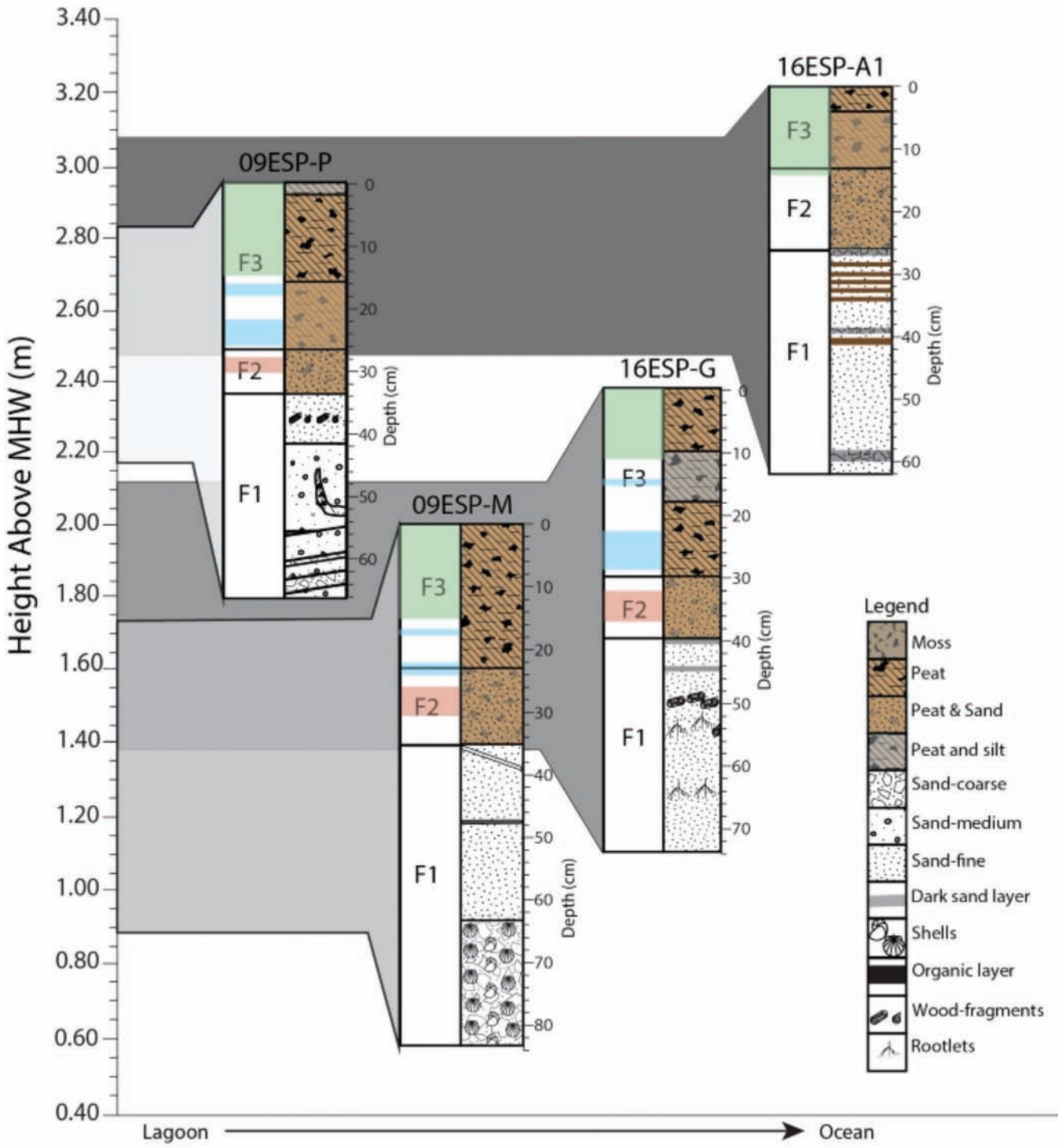

FIG. 2. Stratigraphy and facies designations of the cores studied, ordered vertically by elevation and horizontally by position on the spit from landward to seaward (left to right). Highlighted colours correspond to climatic events: red = Medieval Climate Anomaly, blue = Little Ice Age, green = modern. Symbology adapted from USGS, 2006, FGDC Digital Cartographic Standard for Geologic Map Symbolization.

at the Alaska Stable Isotope Facility at the Water and Environmental Research Center, University of Alaska Fairbanks. Data was obtained with a Thermo Scientific Flash 2000 elemental analyzer and Thermo Scientific ConFlo IV interfaced with a Thermo Scientific DELTA V Plus Mass Spectrometer. Stable isotope ratios were reported in δ notation as parts per thousand (‰) deviation from the international standards VPDB (carbon) and air (nitrogen). Instrument precision for carbon and nitrogen was 0.08‰ and 0.18‰ respectively. Instrument precision for percent carbon and percent nitrogen was 0.29% and 0.26% respectively.

A two end-member mixing model was created for the C:N ratio elemental dataset to determine the organic-matter

TABLE 2. Radiocarbon dates used in this project. Abbreviations are Lab no. for lab number, MHW for mean high water, Cal for calibrated, prob. for probability, and CE for Common Era. All dates are from the National Ocean Sciences Accelerator Mass Spectrometry (NOSAMS) laboratory.

Core ID	Lab no.	Depth in core (cm)	Elevation (m)	Height above MHW (m)	^{14}C Age (14C yr)	Cal CE Median prob. (cal yr)	2σ cal CE Age range (cal yr)	$\delta^{13}C‰$	Δ 14C	Material dated
16ESP-G	OS-147162	24	2.14	1.88	395 ± 15	1469	1448–1616	–27.32	–55.82	Plant/Wood
16ESP-G	OS-132752	36	2.02	1.76	1080 ± 120	952	681–1211	N/A	N/A	Plant/Wood
16ESP-G	OS-132757	37	2.01	1.75	860 ± 50	1185	1044–1270	–26.67	N/A	Plant/Wood
09ESP-M	OS-162312	20.5	1.75	1.49	*N/A	*N/A	*N/A	–25.70	N/A	Plant/Wood
09ESP-M	OS-103631	31	1.69	1.43	1030 ± 25	1010	904–1113	–29.28	N/A	Gramminoid fragments
09ESP-P	OS-162313	27	2.54	2.28	550 ± 20	1402	1325–1424	–26.65	N/A	Plant/Wood/rootlets
09ESP-P	OS-81099	39	2.42	2.16	1520 ± 40	557	433–639	–25.78	–178.9	Terrestrial seeds

*N/A radiocarbon age refers to time post 1950 CE.

source contribution associated with in situ wetland production ($Fraction_{wetland}$) according to

$$C{:}N\ Fraction_{wetland} = \frac{(C{:}N_{sample} - C{:}N_{marine})}{(C{:}N_{wetland} - C{:}N_{marine})}$$

where $C{:}N_{marine}$ is the end member for anticipated inputs from the adjacent ocean ($C{:}N_{marine} = 4$), and $C{:}N_{terrestrial}$ is the end member value for in situ wetland production ($C{:}N_{terrestrial} = 30$) (Wang and Wooller, 2006; De la Vega et al., 2019). These fractional values were graphed through time to show variability of carbon sourcing over paleo and modern time frames.

Dry Bulk and Carbon Density: To produce age-depth models and calculate carbon stocks, we determined the DBD (g/cm^3) and carbon density (CD) for the section of core from which radioisotope data was gathered. DBD was measured on select samples by drying a known volume of sediment to constant weight. Carbon density (gC/cm^3) was calculated by multiplying %C by DBD. Soil carbon stock was calculated by integrating carbon density to basal peat depth. Since DBD and %C sample data were discontinuous, we determined the following relationship between CD and DBD with an r^2 value of 0.81.

$$DBD_{calculated} = -0.263\ln(\%C) + 1.1542$$

Rearranging the equation to solve for %C gave the following equation:

$$\%C_{calculated} = e^{((DBD-1.1542)/-0.263)}$$

This relationship is based on a two-component (e.g., mineral and organic) mixing model description of the relationship between DBD and organic matter in coastal wetland soils (Morris et al., 2016). The above equation is specific to the %C and DBD data of this project and was used to calculate carbon density for depths where either DBD or wt%C was not measured.

Statistics: Statistical tests were used to assess variability in carbon accumulation rates (CAR) between sites and time periods (i.e., paleo and modern). CAR were limited to the Facies 3 (F3) unit (i.e., the unit with the highest organic concentration), as this facies represents wetland environments. The Shapiro-Wilk normality test, Levene's test for homogeneity of variance, descriptive statistics, and the one-way ANOVA analysis of means statistical tests were run for both the paleo and modern groups to analyze the inter-group variability among core locations. Low *p*-values (less than 0.05) for the Shapiro-Wilk and Levene's tests indicate the distribution is not normal and the variance between factors is not equal, respectively. The statistical tests (ANOVA, Wilcoxon rank sum) can operate with data distributions that are mildly to moderately non-normal (Pappas and DePuy, 2004). The paleo and modern CAR datasets were further assessed with a Wilcoxon rank sum test to determine the significance between paleo and

modern CAR. All statistical analyses were completed using the programming language R (v4.2.3; R Core Team 2023).

RESULTS

Core Stratigraphy and Physical and Elemental Data

Three main facies were identified in Cape Espenberg. The stratigraphic order in which facies occurred in each sediment core (i.e., F1 to F2 to F3) was consistent throughout the study site. Physical and elemental data are reported here in conjunction with their facies, as there are significant differences in some datasets between facies types. All data are available in the publication by Maio et al. (2022).

Facies 1 (F1): (F1) was present in all cores; it consisted of well-sorted basal sand deposits ranging from fine to coarse, with wood, shell, and rootlet fragments. Cores 09ESP-M and 09ESP-P showed poor sorting in this facies, with some combination of fine, medium, and coarse grains intermixed. F1 also contained dark organic banding, as seen in core 16ESP-A1 and 16ESP-G. Other than the organic banding in this unit, however, organic materials were limited. Trends in carbon data (very low %C and isotopically heavier $\delta^{13}C$) from F1 suggest marine sources dominate the organic matter (see Table 3). Trends in $\delta^{13}C$ seen among all cores showed heavier isotope values (~ −21‰ to −27‰) combined with very low C content at the bottom of each core (within F1 sand deposits). See Figure 3 and Table 3.

Facies 2 (F2): F2 consisted of intermixed sand and peaty organic materials. Transitions between F1 and F2 were sharp, usually within 2 cm. The peaty organics ranged in colour from light to dark brown and the intermixed sands ranged in colour from medium tan to brown. Some cores demonstrated bands of oxidized rusty colouring. F2 mineral content was well sorted and fine grained. This facies contained some plant macrofossils toward the bottom of the unit.

F2 average $\delta^{13}C$ values were isotopically lighter; the %C and C:N ratio were greater than those found in F1 (Table 3). Results for F2 show a higher DBD than in F3, however, the sample size for density measurements in F2 samples was small (n = 3) versus F3 (n = 57). Additionally, all three DBD samples were collected from core 16ESP-A1, which were the only core density measurements that extended to the depth of F2 (although the F2 facies layer was present in all four cores). The F2 density values for 16ESP-A1 (1.12 g/cm^3, 1.09 g/cm^3, and 1.24 g/cm^3) were taken from a mix of organic and mineral materials.

Facies 3 (F3): F3 occurred directly above F2 and consisted of thick peat with some occurrences of intermixed moss, sand, or silt. Transitions from F2 to F3 ranged from sharp (0 cm−2 cm) to gradual (2 cm−5 cm). Peat deposits consisted of surficial organic material and preserved organic detritus. Intermixed sands were fine grained and well sorted, and silts were very fine grained. Moss layers

TABLE 3. Stable elemental isotope data averages of $\delta^{13}C$, %C, %N, and C:N ratio for F1 through F3 for each of the four cores. Abbreviations are n for sample number, Avg. for average, and sd for standard deviation.

Core ID: 09ESP-M					Core ID: 09ESP-P					Core ID: 16ESP-A1					Core ID: 16ESP-G				
Data type	Facies	n	Avg.	sd	Data type	Facies	n	Avg.	sd	Data type	Facies	n	Avg.	sd	Data type	Facies	n	Avg.	sd
$\delta^{13}C$ (‰, VPDB)	F3	10	− 26.55	0.37	$\delta^{13}C$ (‰, VPDB)	F3	13	− 27.17	0.71	$\delta^{13}C$ (‰, VPDB)	F3	6	− 29.29	0.69	$\delta^{13}C$ (‰, VPDB)	F3	12	-27.02	0.48
	F2	6	− 27.34	0.48		F2	2	− 26.97	0.07		F2	2	− 27.76	0.45		F2	10	-27.13	0.13
	F1	6	− 24.94	2.39		F1	4	− 26.75	0.30		F1	2	− 25.73	0.24		F1	1	-26.82	N/A
%C	F3	10	30.12	5.39	%C	F3	13	33.28	9.39	%C	F3	6	12.17	7.16	%C	F3	12	18.23	5.38
	F2	6	15.38	8.06		F2	2	21.11	11.13		F2	2	2.17	2.66		F2	10	5.23	4.62
	F1	6	0.23	0.12		F1	4	1.97	2.23		F1	2	0.38	0.44		F1	1	0.13	N/A
%N	F3	10	1.78	0.32	%N	F3	13	1.69	0.39	%N	F3	6	0.64	0.40	%N	F3	12	0.84	0.25
	F2	6	0.89	0.49		F2	4	1.19	0.62		F2	2	0.10	0.12		F2	10	0.25	0.21
	F1	6	0.02	0.01		F1	2	0.10	0.10		F1	2	0.02	0.03		F1	1	0.01	N/A
C:N	F3	10	17.00	1.32	C:N	F3	13	19.63	3.60	C:N	F3	6	19.32	1.51	C:N	F3	12	21.60	0.60
	F2	6	17.08	2.13		F2	4	17.79	0.09		F2	2	19.22	3.62		F2	10	21.04	3.49
	F1	6	14.21	2.65		F1	2	16.98	3.91		F1	2	13.52	3.59		F1	1	13.00	N/A

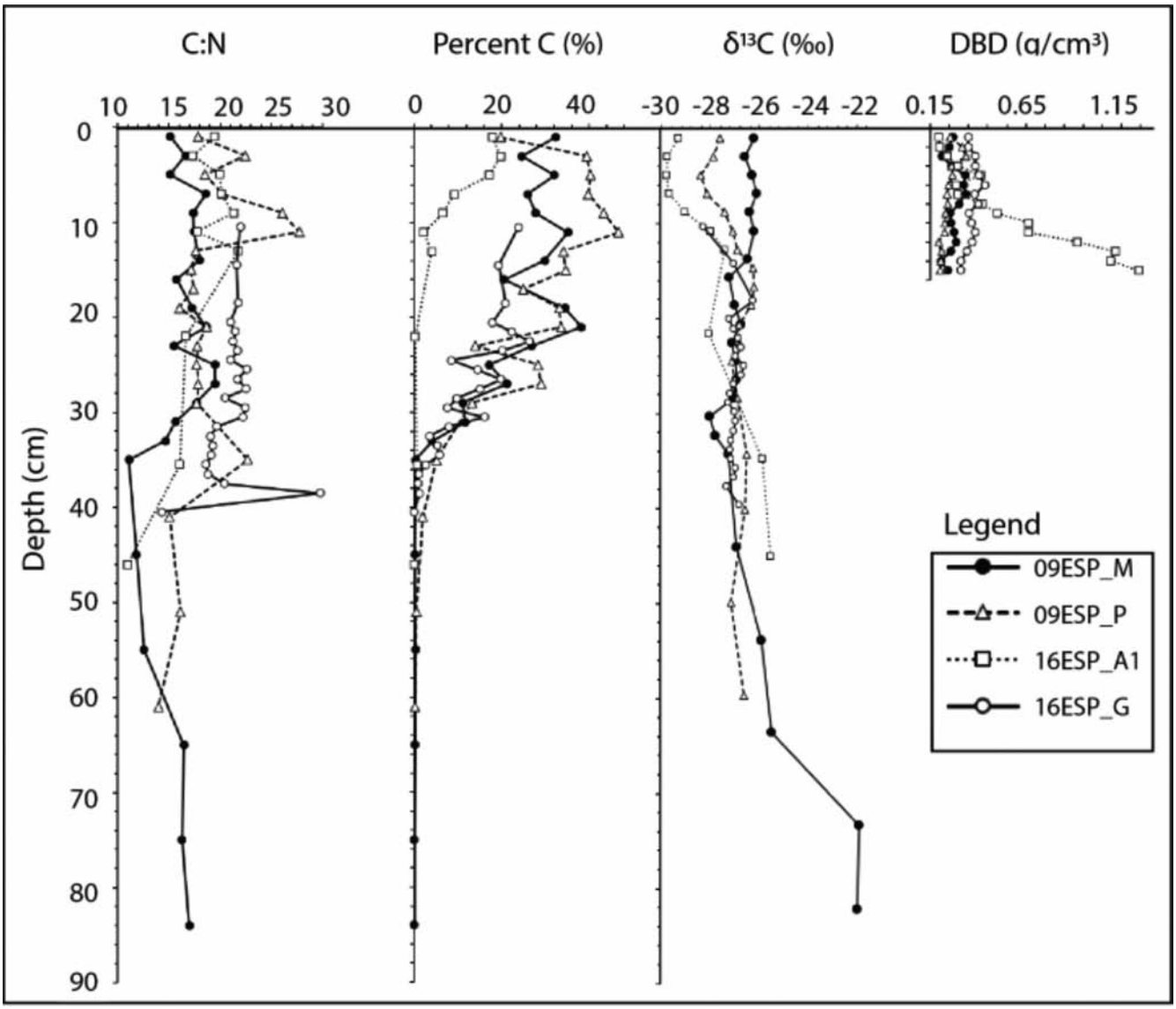

FIG. 3. Stable elemental isotope data through depth (C:N ratio, percent carbon (%C), $\delta^{13}C$ isotope data in VPDB‰, dry bulk density (DBD) in g/cm^3) for Facies 1 through 3.

were characteristically fluffy with lower density than the surrounding peat materials. This facies contained plant macrofossils found throughout the unit.

F3 $\delta^{13}C$ was slightly lighter than F2; it also had the highest %C and C:N ratios, indicating wetland organic matter sources with the least amount of marine organic matter (see Fig. 4, C:N mixing model). Within F3, %C remained low until about the mid- to upper core, where it rapidly increased in value toward the surface to an average of 24.6% ± 9.12% (at depths less than 11 cm).

Elemental Ratio Mixing Model: The isotope mixing model shows a dominance (>50%) of marine carbon sourcing throughout the paleo time frame (Fig. 4). $\delta^{13}C$ showed little variability until approximately 1720 CE, when $Fraction_{terrestrial}$ showed a slight decrease before it increased (from 1920 CE to present) to above 50% terrestrial carbon sourcing. The fractional values for C:N ratio showed more variability through time, with spikes of increased terrestrial fractionation at about 1420 CE, 1530 CE, and 1690 CE. A large spike in marine fractionation was observed at approximately 1900 CE, which then decreased over time as terrestrial fractionation begins to dominate (>50%) at approximately 1980 CE (Fig.4).

Radiometric Dating

Six of the seven ^{14}C dates obtained for this project were used in age modelling (Table 3). One date (core 09ESP-M) appears to be anomalous due to post-1950 CE rootlet contamination and has not been used in generating results. Radiocarbon ages are reported as their calibrated dates in BCE/CE in the following results and discussion. The calendar age range is 1469 CE to 557 CE. The basal peat ages of the cores that yielded dates were 1185 CE (16ESP-G) at 37 cm depth, 1010 CE (09ESP-M) at 31 cm depth, and 557 CE (09ESP-P) at 39 cm depth.

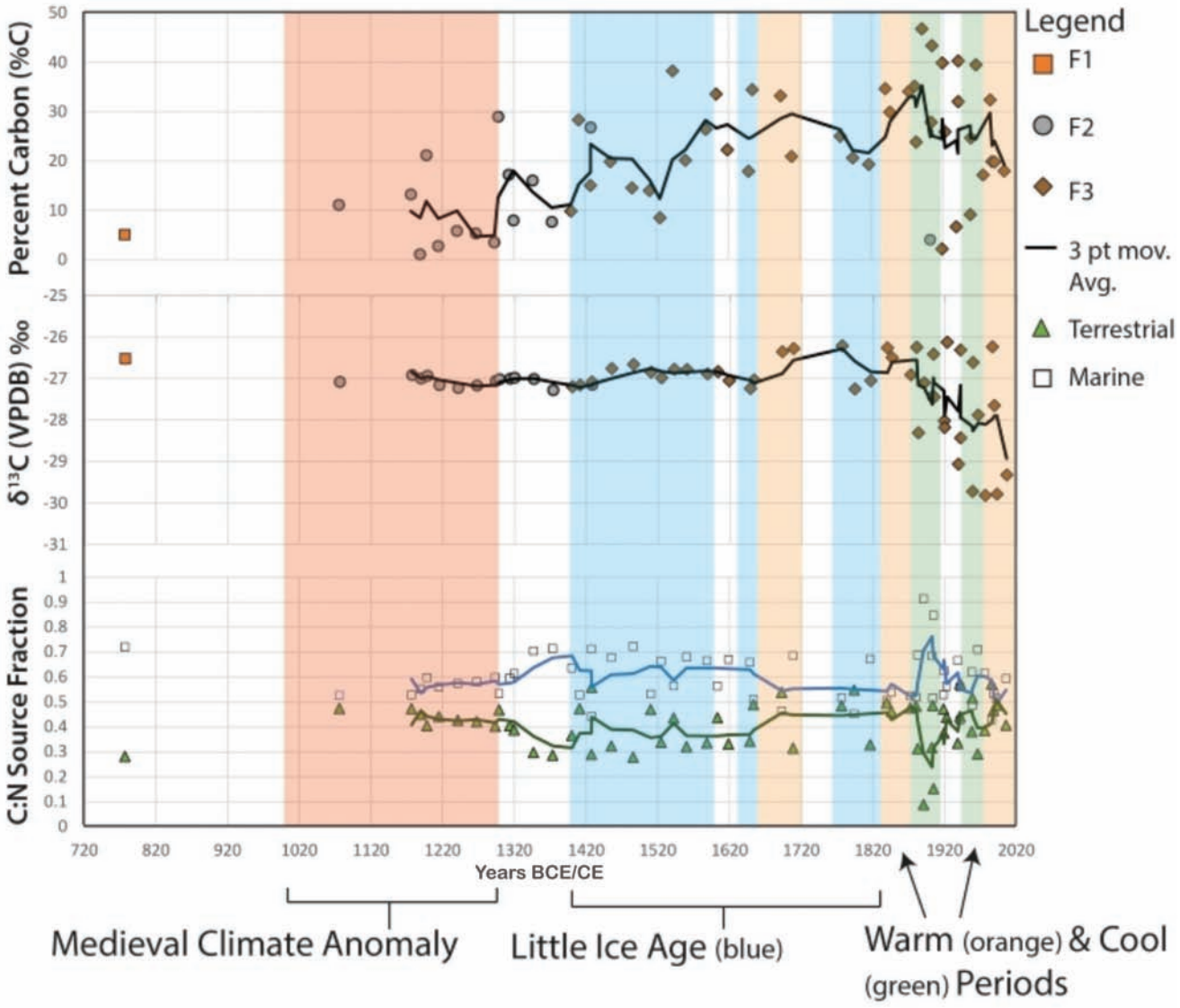

FIG. 4. Elemental data from all four sediment cores used in facies interpretation. The Y-axis is divided into three datasets (from top to bottom): percent carbon, $\delta^{13}C$, and the C:N elemental mixing model. The X-axis is time in CE years. A 3-point moving average is shown by the line in each dataset figure to better illustrate trends over time. The legend provides symbology for Facies 1: F1 (orange square), Facies 2: F2 (grey circle), and Facies 3: F3 (brown diamond) used in the $\delta^{13}C$ and %C data, as well as showing the mixing model symbology of either terrestrial (green triangle) or marine (white square). The MCA is represented by red shading, the LIA is represented by blue shading, and warm and cool periods are orange and green respectively.

The ^{210}Pb depth profiles varied across the four sediment cores (Fig. 5). The $^{210}Pb_{excess}$ inventory was highest in cores 16ESP-A1 and 09ESP-M and lowest in cores 09ESP-P and 16ESP-G; the ^{137}Cs inventory was highest in 09ESP-P and 09ESP-M, intermediate in 16ESP-A1, and lowest in 16ESP-G. Each core expressed a ^{137}Cs peak (Fig. 5) between 1.5 cm and 7.5 cm depths. ^{137}Cs peak depths were shallowest for core 09ESP-P at 1.5 cm, then increased in depth; 09ESP-M was 2.5 cm, 16ESP-G was 4.5 cm, and 16ESP-A1 was 7.5 cm deep (Table 4).

Age-Depth Models and Summary of Accumulation Rates in Facies 3

Age-depth model accuracy depends heavily on the quality and precision of the underlying radioisotope data. We employed rplum, a Bayesian implementation of the continuous rate-of-supply model, that yielded age models spanning all facies (F3 to F1) in all four sediment cores. See supplemental attachment for full model parameters for each core.

Vertical accumulation and carbon burial rate reported values are for the F3 unit unless otherwise stated (Table 5). The average vertical accumulation rate (within F3) for the paleo deposits was 0.28 ± 0.09 mm/yr. Differences within the paleo total mineral and carbon accumulation rates (AR) dataset are statistically significant and large (Table 6; one-way ANOVA test, $p < 0.01$). The distribution of paleo AR values deviated from normality (Shapiro-Wilk test, $p < 0.05$) and were not significantly different in variance between cores (Levene's test, $p = 0.02$).

TABLE 4: Radionuclide inventory of ^{210}Pb, ^{226}Ra, and ^{137}Cs for each core. Cores are organized in order of youngest relative age (top row) to oldest relative age (bottom row). Interval is the depth range for which samples had detectable ^{210}Pb activities. Inventory units are in disintegrations per minute per square centimeter.

Core ID	^{210}Pb inventory (dpm/cm2)	^{226}Ra inventory (dpm/cm2)	^{137}Cs inventory (dpm/cm2)	Interval (cm)
16ESP-A1	20.87	4.33	2.40	0–15
16ESP-G	12.60	1.61	1.82	0–12
09ESP-M	20.94	1.71	3.43	0–15
09ESP-P	14.21	1.05	3.61	0–15

TABLE 5: Vertical accumulation and carbon burial rates. Abbreviations are F3 for facies three, Avg for average, and C for carbon.

Core ID	Data type used	Model type used	F3 Avg modern accumulation rate (mm/yr)	F3 Avg paleo accumulation rate (mm/yr)	F3 Avg modern C burial (gC/m2/yr)	F3 Avg paleo C burial (gC/m2/yr)	Total carbon stocks to basal peat per core (gC/m2)
16ESP-A1	^{210}Pb, ^{137}Cs	CRS	1.30 ± 0.35	n/a	69.9 ± 33.2	n/a	107.5
16ESP-G	^{210}Pb, ^{137}Cs, ^{14}C	CRS	0.80 ± 0.10	0.35 ± 0.05	59.4 ± 7.6	19.9 ± 7.5	167.0
09ESP-M	^{210}Pb, ^{137}Cs, ^{14}C	CRS	0.97 ± 0.23	0.24 ± 0.10	78.3 ± 28.3	18.8 ± 10.4	284.6
09ESP-P	^{210}Pb, ^{137}Cs, ^{14}C	CRS	1.02 ± 0.28	0.23 ± 0.05	84.1 ± 30.8	16.2 ± 4.9	300.9

Of all the sediment cores, 16ESP-A1 has the highest modern vertical accumulation rate and the highest elevation, at 3.08 m above mean high water (MHW). Core 09ESP-M had the lowest elevation (at 1.74 m above MHW) and the second-lowest modern vertical accumulation rate. The average vertical accumulation rate for modern dates was 1.0 ± 0.3 mm/yr. However, the variance among the four sites for AR was statistically significant between sites 16ESP-G and 16ESP-A1 (Table 6; one-way ANOVA, $p < 0.01$). The distribution of modern AR also deviated from normality (Shapiro-Wilk test, $p < 0.05$) and was not significantly different in variance between cores (Table 6; Levene's test, $p = 0.10$). It should be noted that core 16ESP-A1 contains only modern deposits, so paleo dates are not given.

Core 16ESP-G has both the highest paleo vertical accumulation rate and carbon burial rate. The average carbon burial rate prior to 1850 (paleo) was 18.8 ± 7.4 gC/m^2/yr. For the paleo dataset, variations among the three sites that had paleo CAR data were small and not statistically significant (Table 6). Both the Shapiro-Wilk test and Levene's test produced high *p*-values (Table 6).

The average carbon burial rate for modern deposits was 73.5 ± 27.9 gC/m^2/yr. Variation among the four sites for CAR during modern times was not statistically significant (see Table 6). Both the Shapiro-Wilk normality test and Levene's test produced low *p*-values (Table 6).

The depths of peat materials (F3 and F2) for each core were unique. Total carbon stocks were 107.5 gC/m^2 for core 16ESP-A1, 167.0 gC/m^2 for core 16ESP-G, 284.6 gC/m^2 for core 09ESP-M, and 300.9 gC/m^2 for core 09ESP-P (Table 5).

General trends among age-depth models included lower vertical accumulation rates in paleo times, which transitioned abruptly to higher vertical accumulation rates in modern times (e.g. Fig. 5: 09ESP-M vs 16ESP-A1). This sharp break in accumulation rates is common in Bayesian age models with sparse data and no overlap in the shorter-lived ^{210}Pb and longer-lived ^{14}C because the models contain memory down-core when they are implemented. Comparing the paleo to the modern dataset, the Wilcoxon rank sum test with continuity correction produced a low *p*-value ($p < 0.01$), which means that the paleo and modern CAR are statistically significantly different. Additionally,

TABLE 6: Statistical post processing of paleo and modern vertical accumulation and carbon burial rates. A) statistical *p*-values for Levene's test. B) statistical *p*-values and normality distribution for the Shapiro-Wilk test. C) *p*-value for a one way ANOVA test, 95% confident interval (95% CI), effect size squared (Eta2), and signifigance.

A	Levene's test	*p*-value			
	Paleo AR	0.4546			
	Modern AR	0.0996			
	Paleo CAR	0.4529			
	Modern CAR	0.0312			
B	Shapiro-Wilk test	*p*-value	Normalit		
	Paleo AR	0.0002	No		
	Modern AR	0.0191	No		
	Paleo CAR	0.9316	Yes		
	Modern CAR	0.0094	No		
C	ANOVA test	*p*-value	95% CI	Eta2	Significant?
	Paleo AR	< 0.001	[0.22, 1.00]	0.44	Yes
	Modern AR	< 0.001	[0.12, 1.00]	0.31	Yes
	Paleo CAR	0.4776	[0.00, 1.00]	0.05	No
	Modern CAR	0.1020	[0.00, 1.00]	0.12	No

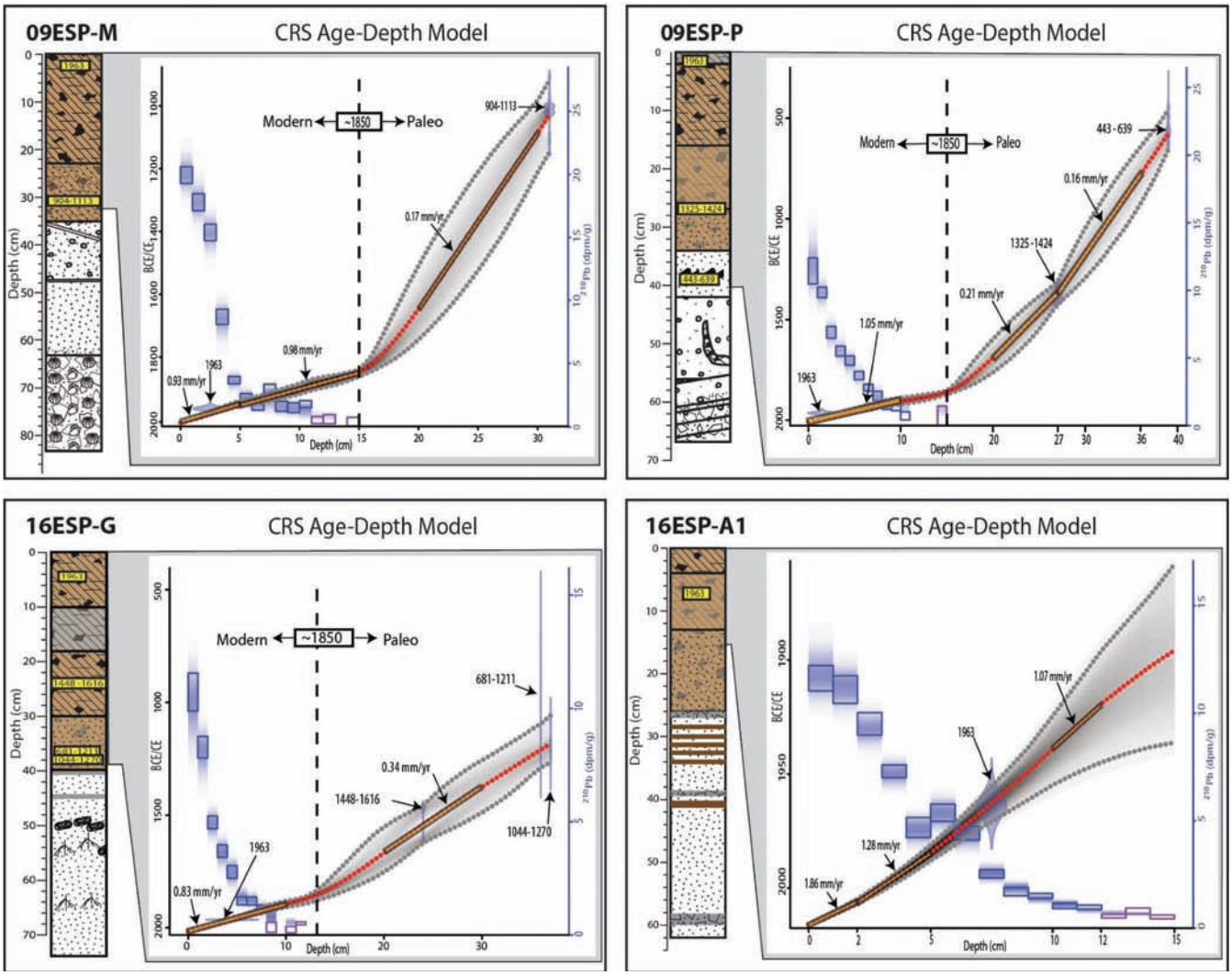

FIG. 5. Integrated figures for each sediment core. Within each core's figure: constant rate of supply (CRS) age-depth model overlaying calibrated dates (blue splotches) and ^{210}Pb levels (blue and purple squares), mean age-depth curve (red line), 95% confidence envelope (grey shading), example slope segment accumulation rates (yellow bars). Depth extent of age-depth models is shown by grey shading connecting the CRS age-depth model to the core log. Core logs show calibrated radiocarbon dates (yellow boxes) in BCE/CE (Cal CE age range). See Figure 2 for stratigraphic symbology legend.

the Wilcoxon rank sum test produced a low p-value ($p < 0.01$), indicating paleo and modern AR are statistically significantly different. Both of these tests illustrate the differences in carbon accumulation and total accumulation rates between the paleo and modern datasets; while CAR showed homogeneity within each climate period (i.e., paleo and modern rates), AR showed variance within each climate period.

DISCUSSION

Cape Espenberg Depositional History

The sediment core logs and proxy data indicate the main depositional environments at Cape Espenberg generally progress from marine sands (F1) to a brackish transition zone of mixed sand and peat (F2) to wetland peat deposits (F3) (Fig. 6).

We interpret F1 as representing a foreshore to a nearshore marine environment actively influenced by coastal processes. It is probable that the genesis of new beach ridges first begins with well-developed offshore sand bars that gain height from aeolian sand deposition and storm debris once they emerge from the active surf zone. As these dunes prograde and are isolated from the coastline, they become stabilized ridges with the establishment of vegetation (Fig. 6).

Evidence for the marine depositional environment of F1 includes coarse sand grains, poor to well sorting, and the presence of wood fragments and marine shells. Storm impacts like surge and overwash provide the energy to deposit coarse grains, wood, and shells. The wood fragments probably originate from abundant driftwood that is present in the system (Giddings, 1952; Alix, 2005; Hellmann et al., 2013). The presence of marine shells is a strong indicator of a marine depositional environment (Mason et al., 1997). Elemental data supports this, as

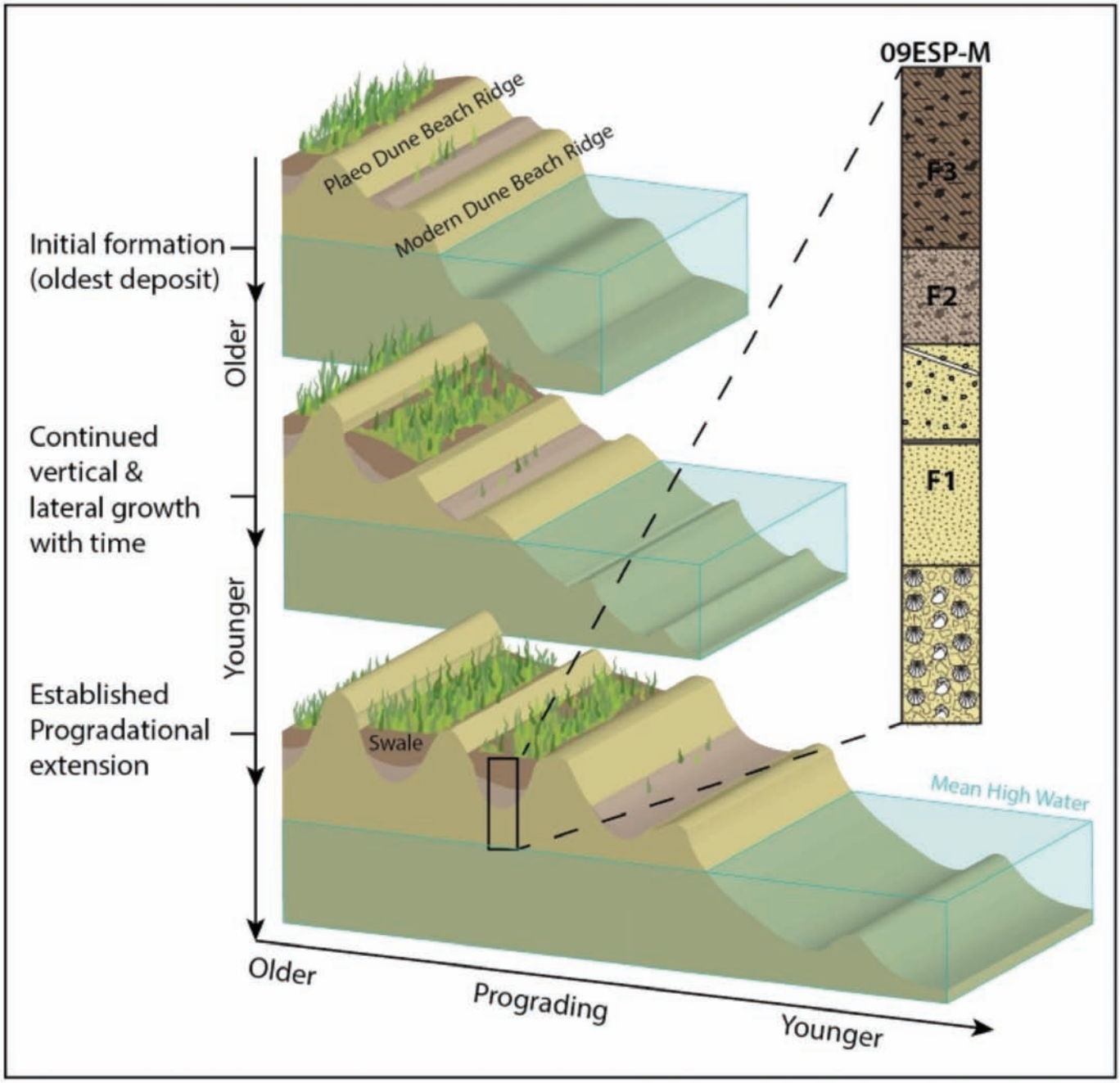

FIG. 6. Conceptual model for the prograding sequences of Cape Espenberg showing multiple stages of spit growth vertically and horizontally through time. Core 09ESP-M is shown to demonstrate a typical coring location and facies distribution within the system. Adapted from Engels and Roberts (2005).

samples from F1 show very low %C values—consistent with marine sands. Additionally, $\delta^{13}C$ values for F1 samples are isotopically heavier, reflecting marine carbon values typical for the Chukchi Sea (Boutton, 1991; Wainright et al., 1998; De la Vega et al., 2019). The mean C:N ratio for F1 is 14.9, falling on the marine side of the mixed carbon source range (Boutton, 1991). The $\delta^{13}C$ value is heavier in F1 than in the overlying units, but the mean $\delta^{13}C$ value is −25.8‰, which suggests less marine influence than indicated by the sand and shells in the sediment. F1 forms the structure needed to support the succeeding F2 and F3 depositional units. The date of transition from F1 to F2 is expressed in one core (09ESP-P), with a range from 844 CE to 909 CE.

As the beach ridge is formed and stabilized, the landward area behind the new beach ridge is sheltered and relatively isolated from coastal processes. This marks the end of F1 and the transition into F2. The increased shelter and the distance from the beach create a brackish environment that fosters deposition of organic material while still receiving some marine sand influence through tidal, storm, and aeolian processes (Fig. 6). F2 consists of medium- to fine-grained marine sand, which indicates a loss of energy compared to F1 (McLaren and Bowles, 1985). F2 also includes intermixed peat and organic material, indicating

the depositional environment is stable enough to support plant growth (Mason et al., 1997). The combination of marine and terrestrial elements suggests a brackish back-dune depositional environment (Fig. 6). Elemental data supports this as the F2 mean $\delta^{13}C$ (-27.3‰) and C:N ratio (19.6) values indicate mixed terrestrial and marine carbon sources (Boutton, 1991; Wang and Wooller, 2006). The date of transition from F2 to F3 varies across the spit with a range of 1299 CE to 1348 CE for core 09ESP-P, 1428 CE to 1486 CE for core 09ESP-M, and 1400 CE to 1428 CE for core 16ESP-G (Fig. 1). This is contrary to the expected progression from the shoreline and is discussed further below.

With the continued progradation of the barrier and further isolation from marine processes, F3 (the most modern deposits at Cape Espenberg) begins to accumulate wetland peat. The generation of a swale behind the beach ridge combined with the gain in elevation of the seaward ridge leads to stabilization of the landscape and long-term peat deposition with very little input of sand or silt. Most sands are fine grained and very well sorted, suggesting aeolian deposition or, in some low-lying areas, possibly marine incursions (Clemmensen et al., 2003). Additionally, the presence of seeds from terrestrial plants (*Sphagnum* sp., *Carex* sp., *Empetrum nigrum*) are indicators of a wetland depositional environment. Elemental data in F3 also indicate predominantly in situ organic matter inputs with the highest carbon concentrations and isotopically light $\delta^{13}C$ values that are typical of C3 terrestrial plants (Wang and Wooller, 2006; Table 2; Fig. 4). The mean C:N ratio for F3 is the highest of all facies (19.63), indicating the most terrestrial carbon sourcing of any unit (Wang and Wooller, 2006; Table 3; Fig. 4).

The locations of cores 16ESP-G and 09ESP-M break the expected progradational rule (for the F2 to F3 transition): that the landward cores (i.e., 09ESP-P, 09ESP-M) have the oldest transition between facies and that the seaward cores (16ESP-G, 16ESP-A1; Fig. 1) have the youngest transition between facies. This lapse in the progradational rule is due to core 16ESP-G having a slightly older F2 to F3 transition than core 09ESP-M. Core 16ESP-G elevation is ~0.4 m higher than core 09ESP-M, which, combined with 09ESP-M's close proximity to surface lakes, suggests that the location around 09ESP-M may have been influenced by a semi-aquatic environment, delaying the transition of F2–F3 deposits. In contrast, the area around core 16ESP-G has a higher elevation and no large lakes in close proximity, potentially allowing F3 deposits to form before the location around core 09ESP-M.

Influence of Climate on Cape Espenberg Wetland Evolution

These sediment records cover periods of enhanced warming (MCA) and cooling (LIA), allowing for the assessment of how changes in temperature influenced the vertical accumulation and carbon burial rates at Cape Espenberg. Paleoclimate records indicate the MCA occurred from 1000 to 1300 CE (D'Arrigo et al., 2005), while the timing of the LIA in the Alaskan Arctic was early 1400s to the mid-1800s, with the coldest year being 1780 CE (D'Arrigo et al., 2005). Additional cool periods occurred in the late 1800s CE to mid-20th century and from the 1960s to early 1990s CE. The LIA (and subsequent cool periods) are interspersed with shorter warm periods that occurred from the mid-1600s to the 1990s CE (highlighted orange in Fig. 4; D'Arrigo et al., 2005). The peak modelled surface air temperature of the MCA occurred from 927 to 936 CE, with a mean temperature reconstruction of 0.48 ± 0.31˚C (Werner et al., 2018). Anomalies in surface air temperature during the cold peaks within the LIA occurred from 1463 to 1472 CE (−1.4 ± 0.2˚C) and from 1811 to 1820 CE (−1.5 ± 0.2˚C; Werner et al., 2018).

Facies evolution during the early MCA started with the onset of peat deposits (F2) about 1060 CE in all cores except for 16ESP-A1 (~10% carbon, C:N terrestrial carbon sourcing of ~43%, and $\delta^{13}C$ isotope range of ~−26.9‰). By the end of the MCA (~1300 CE), %C increased to ~18%. For the period of the MCA, F2 provides the only available datapoints. This could indicate that the warmer conditions during the MCA provided an environmental setting conducive to the onset of peat accumulation at Cape Espenberg, potentially associated with favourable growing conditions—longer growing seasons, warmer temperatures, and wetter conditions (Moore and Knowles, 1989; Yu et al., 2009)—as well as reduced storm activity and shelter from the ocean (Mason et al., 1997), and enhanced peat preservation. The MCA correlates with areas of wide swale building along the centre of the spit.

Facies evolution during the LIA started with the onset of F3 deposits about 1400 CE, with a general increase in percent carbon (~20%), lower (~38%) C:N terrestrial carbon sourcing, and heavier (~−26.8‰) $\delta^{13}C$. The transition between the end of the LIA and the 20th century can be seen in the shift from heavier to lighter $\delta^{13}C$ isotopic values starting in ~1880 CE and extending to ~2005 CE. Additionally, %C increased from ~1918 to ~1986 CE and decreased until ~2005 CE (Fig. 4). Modern warming correlates with a dominance in terrestrial $\delta^{13}C$ values (Fig. 4). Modern warming and possible improved peat and organic growing conditions—from warmer temperatures and longer growing seasons (Chapin et al., 2005)—are probably drivers of the increased terrestrial signature in the mixing model C:N and $\delta^{13}C$ sourcing, as well as the lighter $\delta^{13}C$ isotopic values (which correspond to terrestrial materials). Additionally, the C:N mixing model variability after 1900 CE (except for the cool period peak in marine sourcing about 1880–1900 CE) shows less distinction between the aquatic and terrestrial signatures (Fig. 4), which could reflect more volatile modern climate conditions.

In summary, vertical accumulation rates (total mineral and organic vertical accumulation) within and among the cores have been dynamic through time, as seen in the lower carbon burial and vertical accumulation rates

during paleo times (F1, ~777 CE to 1850 CE), which shift to higher carbon burial and vertical accumulation rates during the modern period (F3, 1850 CE to present). The results indicate that the warmer climate of the MCA (1000 to 1300 CE) was probably conducive to the onset of peat production at Cape Espenberg, which had slightly higher terrestrial signatures until the transition into the LIA about 1400 CE. Paleoclimate conditions within the LIA could have been more limiting towards peat production (i.e., cooler temperatures, less moisture), contributing to less vertical accumulation and lower rates of carbon burial. The transition from the LIA to a warmer modern climate during the past century brought an increase in terrestrial carbon sourcing, probably due to increased terrestrial peat production as a result of the warmer temperatures and longer growing seasons (Chapin et al., 2005) that are more conductive to organic matter accumulation (Gajewski, 2015; Chaudhary et al., 2017; Magnan et al., 2018) than were conditions in the past.

Geomorphic Response to Changes in Storminess Through Time

On Cape Espenberg, the geomorphic response to increases and decreases in storminess can be seen in the response of vertical and carbon accumulation rates and the physical geomorphic structure of the spit itself. Mason et al. (1997) used the geomorphology of the beach-ridge complexes to predict storm activity and noted that periods of increased storminess were associated with higher elevation beach ridges with narrower and fewer peat swales, while a decrease in storminess left a geomorphic signature of lower elevation ridges and wider swales. Thus, on the cape during the LIA, there was an increase in storminess leading to an increase in dune building and decrease in peat formation within the swales, while during the decreased storminess of the MCA, wider swales were developed with increased peat formation (Mason et al., 1997). This can be seen in the low, wide swales around core 09ESP-M versus the high beach ridge and narrow swale around core 16ESP-A1. Another potential driver of the increase in vertical accumulation rates during the modern period is an increase in storminess, though there is an absence of paleo storm records that would allow for that interpretation. Storm surges can transport mineral sediments landward, leading to an increase in sedimentation rates. For example, a major storm event that occurred on 31 December 2016, was documented by Bogardus et al. (2020). During that storm, a 6 m storm surge occurred leading to an ivu (ice pushed onshore from the sea). As part of this surge, sediments were transported up to 120 m landward, leaving fine sand and silt draped over the marsh sediments (Bogardus et al., 2020). Although these types of storms inevitably played some role in the vertical accumulation rates within the cores studied (e.g., the 0.5 to 2 cm of intermixed sand and silt horizons in cores 09ESP-P and 16ESP-G, see stratigraphy), the fact that modern CAR is higher than paleo CAR indicates that the differences may be more related to warmer temperatures and improved growing conditions than a measurable increase in storminess.

RSL Driven Vertical Accumulation Rates: The progradation of Cape Espenberg observed during the late Holocene is dependent on a large source of sediment, its transport northward along the Alaska Coastal Current, and its relative stability in sea levels in the Bering Sea (Mason et al., 1997). Jordan and Mason (2002) estimated relative sea level rise (RSLR) along the eastern Chukchi Sea coast over the past 6000 years was relatively stable at 0.3 mm/yr (~1.5 m total rise over 6000 years), similar to other documented late Holocene sea-level records (Gonneea et al., 2019). When this RSL stability is combined with the continuous supply of sediments being transported from the Yukon River Delta (Brabets et al., 2000; Dornblaser and Striegl, 2009) northward along the Alaska Coastal Current, the barrier has continued to prograde seaward for over 5000 years. However, today global sea levels are rising three to five times faster than during the late Holocene and are projected to continue to increase (Jordan and Mason, 1999; IPCC, 2019; NOAA, 2021).

Although Cape Espenberg does not have a long-running tide station that could be used to assess the rate of RSLR, comparisons can be made using the tide gauge in nearby Nome, Alaska (approximately 250 km to the southwest on Norton Sound, tide station 9468756; NOAA, 2021). Based on the Nome tide gauge data, between 1992 and 2020 the rate of RSLR was 3.89 mm/yr ± 2.7 mm/yr (NOAA, 2021). Despite the large uncertainty and relatively short time scale of this record, there is evidence of a dramatic increase in RSLR in the past 30 years compared to historic rates (e.g., 1992 to 2016 had a total average vertical accumulation of 1.22 ± 0.4 mm/yr), which may have broad implications for the ability of the Cape Espenberg barrier to continue its progradation. Vertical accumulation rates at Cape Espenberg are dynamic and have changed from paleo to modern times. We observed an average 257% increase in vertical accumulation rates between paleo and modern times in all cores except 16ESP-A1, which did not have paleo data. Average CAR increased 291% from paleo to modern times, which indicates that carbon accumulation increased faster than vertical accumulation rates. It is unclear whether wetland accretion will continue to increase to match RSLR. RSLR is an important driver in increasing vertical and carbon accumulation rates associated with an increase in vertical and lateral accommodation space that rising sea-levels create (Gonneea et al., 2019; Rogers et al., 2019; Wang et al., 2021). A mean estimated CAR for the contiguous United States was 161.8 ± 6 gC/m^2/y with 4.2 – 5.0 TgC/yr sequestered across all wetlands, including brackish, tidal freshwater, and mangrove wetlands (Wang et al., 2019). In comparison, the average carbon burial rate (over modern times) at Cape Espenberg is 73.5 ± 27.9 gC/m^2/y. The difference between the two carbon burial rates can probably be attributed to the lower RSLR at Cape Espenberg and the additional differences in regional

climate as a result of latitude. This agrees well with the Wang et al. (2019) study, which found that CAR values decreased with increasing latitude.

In summary, modern carbon and accumulation rates are higher than paleo rates and can be attributed to several factors. These include increasingly optimal peat growing and preservation conditions and an increase in accumulation space from RSLR. An acceleration in RSLR will probably continue to drive CAR at Cape Espenberg in conjunction with current and future warming ground temperatures (e.g., O'Donnell et al., 2012). However, the response of Cape Espenberg coastal wetlands to future RSLR is uncertain. Current hydrologic conditions influenced by persistent permafrost underlying the spit contribute to maintaining low salinity in many of these wetlands. This permafrost creates a perched water table that only experiences minor saline intrusion on the fringes of the spit that are open to the ocean (e.g., the swales open to the ocean on the northeast side). Environmental conditions that cause catastrophic permafrost thaw or salinity intrusion have been shown to negatively impact vertical accumulation in coastal wetlands (O'Donnell et al., 2012; Swindles et al., 2016; Stagg et al., 2017; Zhang et al., 2018). Loss of elevation due to permafrost thaw can result from thermokarst formation (e.g., the collapse of scar bogs, pond and lake formation, taliks; O'Donnell et al., 2012). The impacts of salinity intrusion are more complex than the effects of permafrost thaw. Saline intrusion into fresh systems impacts decomposition by altering physiochemical pathways, biogeochemical functions, and microbial structure, changing the rates of decomposition (Stagg et al., 2017). These responses could potentially reverse the trend of increasing vertical accumulation with the accelerating sea-level rise observed here.

CONCLUSIONS

This study used radioisotope dating techniques (^{210}Pb, ^{137}Cs, and ^{14}C), stable isotope (δ^{13}C) and elemental data (%C, C:N), sediment core logs, and physical data (DBD, CD), to constrain age-depth sequences and reconstruct environmental change through different climate regimes. Cores had three main depositional units: F1 consisted of marine sands and storm debris (shells, wood, large grains); F2 consisted of a transitory brackish back-dune environment with a mix of marine sands and terrestrial peat; F3 consisted of terrestrial stabilization with peat and fine sand horizons or peat and sand mixing. Carbon and mineral accumulation rates have increased from paleo to modern times, indicating that peat and organic materials are more productive or experience less decay under modern climate conditions. Through time, periods of warmer climate (MCA and warm periods in LIA) are associated with greater productivity of terrestrial organic material and slightly isotopically lighter δ^{13}C isotope values and swale formation on the spit. The onset of peat growth at Cape Espenberg coincided with MCA warming. Periods of colder climate (LIA) are associated with increased aquatic organic material sourcing and isotopically heavier δ^{13}C values, as well as dune-ridge formation on the spit and suppression of terrestrial carbon storage. Modern warming is associated with an increase in terrestrial sources of organic matter.

ACKNOWLEDGEMENTS

The major funders of this project include Alaska EPSCoR and the Office of Polar Programs Arctic Natural Science CAREER and NSF-INTERN Supplement awards (Grant #1848542) of the U.S. National Science Foundation (NSF), the Coastal & Marine Hazards and Resources Program of the United States Geological Survey (USGS), and the University of Alaska Fairbanks College of Natural Sciences and Mathematics Department of Geosciences Teaching Assistantship. Any use of trade, firm, or product names is for descriptive purposes only and does not imply endorsement by the U.S. Government. In addition, the NSF Arctic Social Science Birnirk Prehistory project at Cape Espenberg (Grant #1523160) supported this work by providing the sediment cores and datasets (e.g., radiocarbon dates and stable isotope data) analyzed in this project. The NSF Permafrost Coastal Systems Network (1927553). The Birnirk project was also supported by the National Park Service. Additional funding support was provided by the Geological Society of America's Graduate Student Research Grant, the American Geophysical Union's General Student Travel Grant, the University of Alaska Fairbanks' Degree Completion Fellowship, and the Department of Geosciences Brian R. Zelenka Memorial Scholarship. The University of Alaska, Fairbanks, College of Natural Science and Mathematics for supporting open access for this paper.

We thank the communities of Deering, Shishmaref, and Nome for allowing our lab the opportunity to study their ancestral lands. Additional thanks to the National Park Service (Bering Land Bridge National Park and Preserve), the Arctic Coastal Geoscience Lab group, and the USGS lab group located in Woods Hole, Massachusettes, and Dr. Aquino-López for assistance with rplum modelling and code management.

REFERENCES

Alix, C. 2005. Deciphering the impact of change on the driftwood cycle: Contribution to the study of human use of wood in the Arctic. Global and Planetary Change 47:83–98. https://doi.org/10.1016/j.gloplacha.2004.10.004

Appleby, P. 2001. Tracking environmental change using lake sediments. In: Smol, J.P., Birks, H.J.B., Last, W.M., Bradley, R.S., and Alverson, K., eds. Tracking environmental change using lake sediments, Vol. 3. Terrestrial, algal, and siliceous indicators. 171–201. Alphen aan den Rijn: Kluwer Academic Publishers. https://doi.org/10.1007/0-306-47668-1

Aquino-Lopez, M., Blaauw, M., Christen, J.A., and Sanderson, N. 2018. Bayesian analysis of ^{210}pb dating. Journal of Agricultural, Biological and Environmental Statistics 23:317–333. https://doi.org/10.1007/s13253-018-0328-7

Baltas, H., Sirin, M., Dalgic, G., and Cevik, U. 2018. An overview of the ecological half-life of the ^{137}Cs radioisotope and a determination of radioactivity levels in sediment samples after Chernobyl in the eastern Black Sea, Turkey. Journal of Marine Systems 177:21–27. https://doi.org/10.1016/j.jmarsys.2017.09.005

Blaauw, M., and Christen, J.A. 2011. Flexible paleoclimate age-depth models using an autoregressive gamma process. Bayesian Analysis 6(3):457–474. https://doi.org/10.1214/11-BA618

Bogardus, R., Maio, C., Mason, O., Buzard, R., Mahoney, A., and de Wit, C. 2020. Mid-winter breakout of landfast sea ice and major storm leads to significant ice push event along Chuckchi Sea coastline. Frontiers in Earth Science 8: 344. https://doi.org/10.3389/feart.2020.00344

Boutton, T.W. 1991. 11—Stable carbon isotope ratios of natural materials: II. Atmospheric, terrestrial, marine, and freshwater environments. Carbon Isotope Techniques:173–185. https://doi.org/10.1016/B978-0-12-179730-0.50016-3

Brabets, T.P., Wang, B., and Meade, R.H. 2000. Environmental and hydrologic overview of the Yukon River Basin, Alaska and Canada: Water-resources investigations report 99–4204. USGS Science for a Changing World. https://pubs.usgs.gov/wri/wri994204/pdf/wri994204.pdf

Chapin, F.S., Sturm, M., Serreze, M.C., McFadden, J.P., Key, J.R., Lloyd, A.H., McGuire, A.D., et al. 2005. Role of land-surface changes in Arctic summer warming. Science 310(5748):657–660. https://doi.org/10.1126/science.1117368

Chaudhary, N., Miller, P.A., Smith, B. 2017. Modelling past, present and future peatland carbon accumulation across the pan-Arctic region. Biogeosciences 14(18):4023–4044. https://bg.copernicus.org/articles/14/4023/2017/

Chmura, G.L., Anisfeld, S.C., Cahoon, D.R., and Lynch, J.C. 2003. Global carbon sequestration in tidal, saline wetland soils. Global Biogeochemical Cycles 17(4): 1111. https://doi.org/10.1029/2002GB001917

Church, J.A., and White, N.J. 2011. Sea-level rise from the late 19th to the early 20th century. Surveys in Geophysics 32:585–602. https://doi.org/10.1007/s10712-011-9119-1

Clemmensen, L.B, Andreasen, F. Heinemeier, J., and Murray, A. 2003. A Holocene coastal aeolian system, Vejers, Denmark: Landscape evolution and sequence stratigraphy. Terra Nova 13(2):129–134. https://doi.org/10.1046/j.1365-3121.2001.00330.x

Cutshall, N.H., Larsen, I.L., and Olsen, C.R. 1983. Direct analysis of ^{210}Pb in sediment samples: Self-absorption corrections. Nuclear Instruments and Methods in Physics Research 206(1-2):309–312. https://doi.org/10.1016/0167-5087(83)91273-5

D'Arrigo, R., Mashig, E., Frank, D., Wilson, R., and Jacoby, G. 2005. Temperature variability over the past millennium inferred from northwestern Alaska tree rings. Climate Dynamics 24:227–236. https://doi.org/10.1007/s00382-004-0502-1

de la Cruz, E., Gonzalez, R., Klapp, J., Longoria, L.C., Mayoral, E., and Duarte, R. 2011. Numerical simulation of ^{226}Ra migration and decay in a saturated porous medium. Revista Internacional de Contaminación Ambiental 27(3):215–221. https://www.scielo.org.mx/scielo.php?script=sci_arttext&pid=S0188-49992011000300006

de la Vega, C., Jeffreys, R.M., Tuerena, R., Ganeshram, R., and Mahaffey, C. 2019. Temporal and spatial trends in marine carbon isotopes in the Arctic Ocean and implications for food web studies. Global Change Biology 25(12):4116–4130. https://doi.org/10.1111/gcb.14832

Dornblaser, M.M., and Striegl, R.G. 2009. Suspended sediment and carbonate transport in the Yukon River Basin, Alaska: Fluxes and potential future responses to climate change. Water Resources Research 45(6): W06411. https://doi.org/10.1029/2008WR007546

Douglas, B.C. 1991. Global sea level rise. Journal of Geophysical Research: Oceans 96 (C4):6981–6992. https://doi.org/10.1029/91JC00064

Engels, S., and Roberts, M.C. 2005. The architecture of prograding sandy-gravel beach ridges formed during the last Holocene highstand: Southwestern British Columbia, Canada. Journal of Sedimentary Research 75(6):1052–1064. https://doi.org/10.2110/jsr.2005.081

Fargione, J.E., Bassett, S. Boucher, T., Bridgham, S.D., Conant, R.T., Cook-Patton, S.C., Ellis, P.W., et al. 2018. Natural climate solutions for the United States. Science Advances 4(11): eaat1869. https://doi.org/10.1126/sciadv.aat1869

Farquharson, L.M., Mann, D.H., Swanson, D.K., Jones, B.M., Buzard, R.M., and Jordan, J.W. 2018. Temporal and spatial variability in coastline response to declining sea-ice in northwest Alaska. Marine Geology 404:71–83. https://doi.org/10.1016/j.margeo.2018.07.007

Flagstad, L., Steer, A., Boucher, T. Aisu, M., and Lema, P. 2018. Wetlands across Alaska: Statewide wetland map and assessment of rare wetland ecosystems. Alaska Natural Heritage Program. Alaska Center for Conservation Science, University of Alaska. https://accscatalog.uaa.alaska.edu/sites/default/files/FlagstadEtAl2018_WetlandsAcrossAlaska.pdf

Ford, J., and Pearce, T. 2009. What we know, do not know, and need to know about climate change vulnerability in the western Canadian Arctic: A systematic literature review. Environmental Research Letters 5(1): 014008. https://doi.org/10.1088/1748-9326/5/1/014008

Gajewski, K. 2015. Impact of Holocene climate variability on Arctic vegetation. Global and Planetary Change 133:272–287. https://doi.org/10.1016/j.gloplacha.2015.09.006

Giddings, J.L. 1952. Driftwood and problems of Arctic sea currents. Proceedings of the American Philosophical Society 96(2):129–142. https://www.jstor.org/stable/3143719

———. 1967. Ancient men of the Arctic. New York: Knopf. https://archive.org/details/ancientmenofarct00gidd

Giddings, J., and Anderson, D.D. 1986. Beach ridge archaeology of Cape Krusenstern, Eskimo and Pre-Eskimo settlements around Kotzebue Sound, Alaska. Publications in Archeology, tDAR id: 93089. https://api.semanticscholar.org/CorpusID:127534578

Gonneea, M., Maio, C., Kroeger, K., Hawkes, A., Mora, J., Sullivan, R., Madsen, S., Buzard, R., Cahill, N., and Donnelly, J. 2019. Salt marsh ecosystem restructuring enhances elevation resilience and carbon storage during accelerating relative sea-level rise. Estuarine, Coastal and Shelf Science 217:56–68. https://doi.org/10.1016/j.ecss.2018.11.003

Gornitz, V. 1995. A comparison of differences between recent and Late Holocene sea-level trends from eastern North America and other selected regions. Journal of Coastal Research. Special Issue 17:287–297. https://www.jstor.org/stable/25735656

Hagedorn, B., Aalto, R., Sletten, R.S., and Hallet, B. 2008. Frost boil dynamics using ^{210}Pb as a tracer for soil movement. Proceedings of the Ninth International Conference on Permafrost, 28 June–3 July 2008. Fairbanks, Alaska 2:613–618. https://www.researchgate.net/publication/236896473_Frost_boil_dynamics_using_210_Pb_as_a_tracer_for_soil_movement

Harritt, R. 1994. Eskimo prehistory on the Seward Peninsula, Alaska. Resources Report NPS/ARORCR/CRR-93/21. Anchorage: National Park Service, U.S. Department of the Interior.

Hellmann, L., Tegel, W., Eggertsson, O., Schweingruber, F.H., Blanchette, R., Kirdyanov, A., Gärtner, H., and Büntgen, U. 2013. Tracing the origin of Arctic driftwood. Journal of Geophysical Research: Biogeosciences 118(1):68–76. https://doi.org/10.1002/jgrg.20022

Holmquist, J.R., Windham-Myers, L., Bernal, B., Byrd, K.B., Crooks, S., Gonneea, M.E., Herold, N., et al. 2018. Uncertainty in United States coastal wetland greenhouse gas inventorying. Environmental Research Letters 13(11): 115005. https://doi.org/10.1088/1748-9326/aae157

Hughes, O., and Terasmae, J. 1963. SIPRE ice-corer for obtaining samples from permanently frozen bogs. Arctic 16(4):270–272. https://doi.org/10.14430/arctic3547

IPCC (Intergovernmental Panel on Climate Change). 2022. Summary for policymakers. In: Abram, N., Adler, C., Bindoff, N.L., Cheng, L., Cheong, S., Cheung, W.W.L., Collins, M., et al. The ocean and cryosphere in a changing climate: Special report of the Intergovernmental Panel on Climate Change. https://doi.org/10.1017/9781009157964.001

———. 2023. Climate change 2021—The physical science basis: Working Group I contribution to the sixth asssessment report of the intergovernmental panel on climate change. Cambridge: Cambridge University Press. https://doi.org/10.1017/9781009157896

Jordan, J., and Mason, O. 1999. A 5000 year record of intertidal peat stratigraphy and sea level change from northwest Alaska. Quaternary International 60(1):37–47. https://doi.org/10.1016/S1040-6182(99)00005-1

———. 2002. Minimal Late Holocene sea level rise in the Chukchi Sea: Arctic insensitivity to global change? Global and Planetary Changes 32(1):13–23.
https://doi.org/10.1016/S0921-8181(01)00146-1

Kåresdotter, E., Destouni, G., Ghajarnia, N., Hugelius, G., and Kalantari, Z. 2021. Mapping the vulnerability of Arctic wetlands to global warming. Earth's Future 9(5): e2020EF001858.
https://doi.org/10.1029/2020EF001858

Lindsey, R. 2020. Climate change: Global sea level. NOAA Climate.gov.
https://www.climate.gov/news-features/understanding-climate/climate-change-global-sea-level

Magnan, G., van Bellen, S., Davies, L., Froese, D., Garneau, M., Mullan-Boudreau, G., Zaccone, C., and Shotyk, W. 2018. Impact of the Little Ice Age cooling and 20th century climate change on peatland vegetation dynamics in central and northern Alberta using a multi-proxy approach and high-resolution peat chronologies. Quaternary Science Reviews 185:230–243.
https://doi.org/10.1016/j.quascirev.2018.01.015

Mahoney, A.R., Eicken, H., Gaylord, A.G., and Gens, R. 2014. Landfast sea ice extent in the Chukchi and Beaufort Seas: The annual cycle and decadal variability. Cold Regions Science and Technology 103:41–56.
https://doi.org/10.1016/j.coldregions.2014.03.003

Maio, C., Smith, L., Meagan E., and Bigelow, N. 2022. Sediment core data from Cape Espenberg, Alaska, 2018–2022. Arctic Data Center.
https://doi.org/10.18739/A2GH9BB73

Mason, O. 1990. Beach ridge geomorphology of Kotzebue Sound: Implications for paleoclimatology and archaeology. Ph.D. dissertation, University of Alaska Fairbanks, Fairbanks.
http://hdl.handle.net/11122/9339

Mason, O.K, Hopkins, D.M., and Plug, L. 1997. Chronology and paleoclimate of storm-induced erosion and episodic dune growth across Cape Espenberg spit, Alaska, U.S.A. Journal of Coastal Research 13(3):770–797.
https://www.jstor.org/stable/4298672

Mason, O.K., Jensen, A.M., Rinck, B., Alix, C.M., Bowers, P.M., and Hoffecker, J.F. 2020. Heightened early medieval storminess across the Chukchi Sea, AD 400–1100: A proxy of the late antique Little Ice Age.Quaternary International 549:98–117.
https://doi.org/10.1016/j.quaint.2019.01.042

McLaren, P., and Bowles, D. 1985. The effects of sediment transport on grain-size distributions. Journal of Sedimentary Research 55(4):457–470.
https://pubs.geoscienceworld.org/sepm/jsedres/article/55/4/457/97803/The-effects-of-sediment-transport-on-grain-size

McLaughlin, J., and Webster, K. 2014. Effects of climate change on peatlands in the far north of Ontario, Canada: A synthesis. Arctic, Antarctic, and Alpine Research 46(1):84–102.
https://doi.org/10.1657/1938-4246-46.1.84

Moore, T., and Knowles, R. 1989. The influence of water table levels on methane and carbon dioxide emissions from peatland soils. Canadian Journal of Soil Science 69(1):33–38.
https://doi.org/10.4141/cjss89-004

Morris, J.T., Barber, D.C., Callaway, J.C., Chambers, R., Hagen, S.C., Hopkinson, C.S., Johnson, B.J., et al. 2016. Contributions of organic and inorganic matter to sediment volume and accretion in tidal wetlands at steady state. Earth's Future 4 (4):110–121.
https://doi.org/10.1002/2015EF000334

Murray, N.J., Worthington, T.A., Bunting, P., Duce, S., Hagger, V., Lovelock, C.E., Lucas, R., et al. 2022. High-resolution mapping of losses and gains of Earth's tidal wetlands. Science 376(6594):744–749.
https://doi.org/10.1126/science.abm9583

Myers-Smith, I.H., Elmendorf, S.C., Beck, S.A., Wilmking, M., Hallinger, M., Daan, B., Tape, K.D., et al. 2015. Climate sensitivity of shrub growth across the tundra biome. Nature Climate Change 5:887–891.
https://doi.org/10.1038/nclimate2697

NOAA (National Oceanic and Atmospheric Administration). 2021. NOAA tides & currents: Relative sea level trends. Nome, Alaska.
https://tidesandcurrents.noaa.gov/sltrends/

Norman, L.E.Y., Friesen, M.T., Alix, C., O'Rourke, M.J.E., and Mason, O.K. 2017. An early Inupiaq occupation: Observations on a Thule house from Cape Espenberg, Alaska. Open Archaeology 3:17–48.
https://doi.org/10.1515/opar-2017-0002

O'Donnell, J.A., Jorgenson, M.T., Harden, J.W., McGuire, A.D., Kanevskiy, M.Z., and Wickland, K.P. 2012. The effects of permafrost thaw on soil hydrologic, thermal, and carbon dynamics in an Alaskan Peatland. Ecosystems 15:213–229.
https://doi.org/10.1007/s10021-011-9504-0

Osland, M.J., Chivoiu, B., Enwright, N.M., Thorne, K.M., Guntenspergen, G.R., Grace, J.B., Dale, L.L., et al. 2022. Migration and transformation of coastal wetlands in response to rising seas. Science Advances 8(26): eabo5174.
https://doi.org/10.1126/sciadv.abo5174

Pappas, P., and DePuy, V. 2004. An overview of non-parametric tests in SAS®: When, why, and how. Proceeding of the South East SAS Users Group Conference (SESUG 2004): Paper TU04.
https://analytics.ncsu.edu/sesug/2004/TU04-Pappas.pdf

Pirazzoli, P. 1991. Part 2: Regional sea-level changes. Elsevier Oceanography Series 58:33–227.
https://doi.org/10.1016/S0422-9894(08)70593-2

Plug, L.J. 2003. Ground-ice features and depth of peat across a mire chronosequence, NW Alaska. In: Phillips, M., Springman, S.M., and Arenson, L.U., eds. Lisse: Swets & Zeitlinger. 901–906.
https://www.arlis.org/docs/vol1/ICOP/55700698/Pdf/Chapter_158.pdf

R Core Team. 2023. R: A language and environment for statistical computing reference index. Version 4.6.0. Vienna, Austria.
https://lib.stat.cmu.edu/R/CRAN/doc/manuals/r-devel/fullrefman.pdf

Reimer, P.J., Austin, W.E.N., Bard, E., Bayliss, A., Blackwell, P.G., Bronk Ramsey, C., Butzin, M., et al. 2020. The Intcal20 northern hemisphere radiocarbon age calibration curve (0–55 cal kBP). Radiocarbon 62(4):725–757.
https://doi.org/10.1017/S0033822200013904

Rogers, K., Kelleway, J.J., Saintilan, N., Megonigal, J.P., Adams, J.B., Holmquist, J.R., Lu, M., et al. 2019. Wetland carbon storage controlled by millennial-scale variation in relative sea-level rise. Nature 567:91–95.
https://doi.org/10.1038/s41586-019-0951-7

Schaaf, J. 1988. Bering Land Bridge National Preserve: An archaeological survey, Vol. I. Site descriptions. Anchorage: National Park Service, U.S. Department of the Interior.
https://www.npshistory.com/series/archeology/bering/1/report.pdf

Seifollahi-Aghmiuni, S., Kalantari, Z., Land, M., and Destouni, G. 2019. Change drivers and impacts in Arctic wetland landscapes—Literature review and gap analysis. Water 11(4): 722.
https://doi.org/10.3390/w11040722

Serreze, M.C., and Barry, R.G. 2011. Processes and impacts of Arctic amplification: A research synthesis. Global and Planetary Change 77(1):85–96.
https://doi.org/10.1016/j.gloplacha.2011.03.004

Smith, M.A., Goldman, M.S., Knight, E.J., and Warrenchuk, J.J. 2017. Ecological atlas of the Bering, Chukchi, and Beaufort Seas 2nd edition. Anchorage: Audubon Alaska.
https://ak.audubon.org/conservation/download-ecological-atlas-bering-chukchi-and-beaufort-seas

Stagg, C.L., Schoolmaster, D.R., Krauss, K.W., Cormier, N., and Conner, W.H. 2017. Causal mechanisms of soil organic matter decomposition: Deconstructing salinity and glooding impacts in coastal wetlands. Ecology 98(8):2003–2018.
https://doi.org/10.1002/ecy.1890

Swindles, G.T, Morris, P.J, Mullan, D., Watson, E.J., Turner, T.E., Roland, T.P., Amesbury, M.J., et al. 2016. The long-term fate of permafrost peatlands under rapid climate warming. Scientific Reports 5: 17951.
https://doi.org/10.1038/srep17951

Tape, K., Sturm, M., and Racine, C. 2006. The evidence for shrub expansion in northern Alaska and the pan-Arctic. Global Change Biology 12(4):686–702.
https://doi.org/10.1111/j.1365-2486.2006.01128.x

Tootchi, A., Jost, A., and Ducharne, A. 2019. Multi-source global wetland maps combining surface water imagery and groundwater constraints. Earth System Science Data 11(1):189–220.
https://doi.org/10.5194/essd-11-189-2019

Urban, T.M., Rasic, J.T., Alix, C. Anderson, D.D. Manning, S.W., Mason, O.K., Tremayne, A.H., and Wolff, C. 2016. Frozen: The potential and pitfalls of ground-penetrating radar for archaeology in the Alaskan Arctic. Remote Sensing 8(12): 1007.
https://doi.org/10.3390/rs8121007

U.S. NPS (U.S. National Park Service). 2015. Bering land bridge: History & culture.
https://home.nps.gov/bela/learn/historyculture/index.htm

USGS (U.S. Geological Survey). 2006. FGDC digital cartographic standard for geologic map symbolization (postscript implementation). Techniques and Methods 11-A2. USGS Science for a Changing World.
https://doi.org/10.3133/tm11A2

Voltaggio, M., and Spadoni, M. 2011. Direct determination of half-life of ^{214}Pb by gamma spectrometry and comparison with previous indirect measurements. Applied Radiation and Isotopes 69(4):705—710.
https://doi.org/10.1016/j.apradiso.2010.12.014

Wainright, S.C., Haney, J.C., Kerr, C., Golovkin, A.N., and Flint, M.V. 1998. Utilization of nitrogen derived from seabird guano by terrestrial and marine plants at St. Paul, Pribilof Islands, Bering Sea, Alaska. Marine Biology: International Journal of Life and Oceans and Coastal Waters 131:63–71.
https://doi.org/10.1007/s002270050297

Wang, F., Lu, X., Sanders, C.L., and Tang, T. 2019. Tidal wetland resilience to sea level rise increases their carbon sequestration capacity in United States Nature Communications 10: 5434.
https://doi.org/10.1038/s41467-019-13294-z

Wang, F., Sanders, C.J., Santos, I.R., Tang, J., Schuerch, M., Kirwan, M.L., Kopp, R.E., et al. 2021. Global blue carbon accumulation in tidal wetlands increases with climate change. National Science Review 8(9): nwaa296.
https://doi.org/10.1093/nsr/nwaa296

Wang, Y., and Wooller, M.J. 2006. The stable isotopic (C and N) composition of modern plants and lichens from northern Iceland: With ecological and paleoenvironmental implications. Jokull 56:27–37.
https://doi.org/10.33799/jokull2006.56.027

Ward, R.D. 2020. Carbon sequestration and storage in Norwegian Arctic coastal wetlands: Impacts of climate change. Science of The Total Environment 748: 141343.
https://doi.org/10.1016/j.scitotenv.2020.141343

Wassmann, P., Duarte, C.M., Agusti, S., and Sejr, M.K. 2010. Footprints of climate change in the Arctic marine ecosystem. Global Change Biology 17(2):1235–1249.
https://doi.org/10.1111/j.1365-2486.2010.02311.x

Werner, J.P., Divine, D.V., Ljungqvist, F.C., Nilsen, T., and Francus, P. 2018. Spatio-temporal variability of Arctic summer temperatures over the past 2 millenia. Climate of the Past 14(4):527–557.
https://doi.org/10.5194/cp-14-527-2018

WHOI (Woods Hole Oceanographic Institution). 2015. About national ocean sciences accelerator mass spectrometry (NOSAMS).
https://www2.whoi.edu/site/nosams/about/

Willingham, A. 2018. Bering land bridge: Official visitor's guide. Nome, Alaska: National Parks Service.
https://www.nps.gov/bela/planyourvisit/upload/BELAVistorsGuide_ForWeb_2017–508.pdf

Yu, Z., Beilman, D.W., and Jones, M.C. 2009. Sensitivity of northern peatland carbon dynamics to Holocene climate change. In: Baird, A.J., Belyea, L.R., Comas, X., Reeve, A.S., and Slater, L.D., eds. Carbon Cycling in Northern Peatlands 184:55–69.
https://doi.org/10.1029/2008GM000822

Zhang, H., Gallego-Sala, A.V., Amesbury, M.J., Charman, D.J., Piilo, S.R., and Valiranta, M.M. 2018. Inconsistent response of Arctic permafrost peatland carbon accumulation to warm climate phases. Global Biogeochemical Cycles 32(10):1605–1620.
https://doi.org/10.1029/2018GB005980